Shell-confined atom and plasma: Incidental degeneracy, metallic character, and information entropy

Neetik Mukherjee [*] and Amlan K. Roy [†]
Department of Chemical Sciences, Indian Institute of Science Education and Research Kolkata, Mohanpur 741246, Nadia, West Bengal, India

(Received 12 July 2021; accepted 22 September 2021; published 6 October 2021)

Shell-confined atoms can serve as a generalized model to explain both the *free* and *confined* conditions. In this scenario, an atom is trapped inside two concentric spheres of inner (R_a) and outer (R_b) radii. The choice of R_a and R_b renders four different quantum-mechanical systems. In hydrogenic atoms, they are termed (i) the free hydrogen atom (FHA), (ii) the confined hydrogen atom, (iii) the shell-confined hydrogen atom (SCHA), and (iv) the left-confined hydrogen atom (LCHA). By placing R_a and R_b at the location of radial nodes of respective *free* n and ℓ states, a new kind of degeneracy may arise. At a given n of the FHA, $\frac{n(n+1)(n+2)}{6}$ isoenergic states with energy $-\frac{Z^2}{2n^2}$ exist. Furthermore, within a given n, the individual contribution of each of these four potentials has also been enumerated. This incidental degeneracy concept is further explored and analyzed in certain well-known *plasma* (Debye and exponential-cosine-screened) systems. Multipole oscillator strength $f^{(k)}$ and polarizability $\alpha^{(k)}$ are evaluated for systems (i)–(iv) in some low-lying states ($k = 1-4$). In excited states, *negative* polarizability is also observed. In this context, the metallic behavior of H-like systems in the SCHA is discussed and demonstrated. Additionally, analytical closed-form expression of $f^{(k)}$ and $\alpha^{(k)}$ are reported for $1s, 2s, 2p, 3d, 4f, 5g$ states of the FHA. Finally, Shannon entropy and Onicescu information energies are investigated in ground states in the SCHA and LCHA in both position and momentum spaces.

DOI: 10.1103/PhysRevA.104.042803

I. INTRODUCTION

The discovery and development of modern scientific techniques have triggered intense interest in confined quantum systems. Particularly, in such an environment, the rearrangement of atomic orbitals and the increase in the coordination number may lead to some fascinating, exceptional changes in the physical and chemical characteristics [1], such as room-temperature superconductivity [2], metallic behavior in the ground state of H-like atoms [3], etc. These confined systems have profound applications in condensed-matter physics, high-energy physics, astrophysics, and nanotechnology [4,5]. The idea of quantum confinement has been exploited in the construction of an *artificial atom* or a *quantum dot* [6]. Such systems typically consist of a group of electrons confined within a potential well. Another important example is the encapsulation of an atom or molecule in a fullerene cage or zeolite cavity [7–9].

Atomic polarization plays a key role in explaining a number of processes in physics and chemistry. For example, multipole polarizability of an atom reflects quantitative distortion in the electronic charge distribution due to the presence of an external electromagnetic field. A host of macroscopic properties like the refractive index and dielectric constant can be estimated via dipole polarizability [10]. The latter plays an important role in the determination of physicochemical properties, like optical response, as well as atomic and molecular interactions [11].

Originally, the confinement model was proposed to understand changes in the static dipole polarizability of H atoms due to the influence of effective pressure acting on a given surface [12]. In this fundamental system, a H atom was trapped inside an impenetrable spherical cavity. The results of the designed model were utilized to gain knowledge about the cores of planets like Jupiter and Saturn [13,14]. Of late, this concept has been extended to a number of other physical, chemical, and biological systems. A considerable amount of theoretical work has been published, covering a large variety of confining potentials [1,4], resulting in a vast literature. A confined H atom (CHA) in a spherical enclosure [15–22] represents a prototypical system whose Schrödinger equation (SE) can be solved *exactly* [17,23] in terms of the *Kummer confluent hypergeometric* function. A hydrogen atom under the influence of several *penetrable* and *impenetrable* cavities was explored with great enthusiasm, giving rise to several interesting attractive properties from both chemical and physical points of view. They offer some unique phenomena, especially the rearrangement of atomic orbitals and *simultaneous, incidental*, and *interdimensional* degeneracies [23]. Recently, a virial-like theorem was also formulated for such a confinement situation [24]. Moreover, various properties, such as the hyperfine splitting constant, dipole shielding factor, nuclear magnetic screening constant, static and dynamic polarizabilities, information entropy, and Compton profiles [25–31], were examined for a CHA. Further, information-theoretic measures were investigated for H-like atoms in Debye plasmas [32]. A recent study reported the influence of external electric field on total Shannon entropy S_t [33]. Benchmark results for Rényi

[*]pchem.neetik@gmail.com
[†]Corresponding author: akroy@iiserkol.ac.in, akroy6k@gmail.com

and Tsallis entropies and Onicescu information energy E^O for the ground state of a helium atom were studied using Hylleraas's method [34]. The static multipole polarizabilities are estimated for H-like atoms using Hulthén's potential under both *confined* and *free* conditions [35] and for H atoms in ring-shaped potentials [36]. Moreover, the generalized pseudospectral (GPS) method was used to explore several spectroscopic properties such as fine structure and hyperfine splitting in a confined environment [37]. Photoionization in H atoms in a fullerene cage was also reported for low-lying s states [38]. However, an in-depth analysis of multipole oscillator strength and polarizability has yet to be done for H atoms trapped inside a cage, which is one of the objectives of this work.

A shell-confinement model provides a new, unique boundary condition [3,39,40]. An appropriate choice of inner (R_a) and outer (R_b) radii of the shell can describe all possible radial boundary conditions reported so far in the literature. For instance, when $R_a = 0, R_b = r_c$ (r_c is a real finite number), the shell confined model reduces to the CHA. On the other hand, for $R_a = 0, R_b = \infty$, a *free* H atom (FHA) is achieved. When both R_a and R_b are nonzero and finite, the atom is called a *shell-confined H-like atom* (SCHA). However, a *finite* R_a and *infinite* R_b indicate a *left-confined H-like atom* (LCHA). All these four systems, in general, are referred to as a *generalized confined H atom* (GCHA). The nodal characteristics of orbitals of a FHA have played a significant role in the conceptual development of degeneracy in the GCHA. Previously, an attempt was made to solve the SE of the SCHA *exactly* [40], with limited success. Later, an accurate numerical strategy [3,41] was prescribed to emphasize the occurrence of incidental degeneracy in a SCHA [39]. This new degeneracy can also account for the presence of incidental and simultaneous degeneracy in a CHA. The Kirkwood [42] and Buckingham [43] polarizabilities were evaluated [39]. Sternheimer's perturbation-numerical method [44] was employed to calculate the dipole polarizability in the ground state [39]. Buckingham's results are in good agreement with the polarizability obtained via the perturbation-numerical procedure [3]. The higher value of the dipole polarizability in the SCHA indicates metallic behavior of the H atom in the ground state [3]. Eigenvalues and eigenfunctions of a D-dimensional SCHA were examined recently [45].

In practice, a prototypical example of shell confinement is the encapsulation of an atom or molecule in a fullerene cage and zeolite cavity [46] or inside a *metal-organic framework* [47,48]. Such an environment enhances the stability and activity of *noble*-metal catalysts by inhibiting the sintering effect [48–52], amplifies photoluminescence in nanocrystals by reducing nonradiative Auger processes [47,53], and removes defects in polymer crystals [54,55]. Apart from these examples, shell confinement has potential applications in pollution control [56,57], therapeutics [58], and energy storage [59–61].

In spite of having such versatile characteristics, the shell-confinement model has been studied only sparingly. As a consequence, literature on the topic is rather scarce. In this article, our primary objective is to explore SCHAs systematically, mainly through energy and other characteristic properties. Towards this goal, we consider incidental degeneracy, multipole (2^k-pole) oscillator strength $f^{(k)}$, and polarizability $\alpha^{(k)}$ ($k = 1 - 4$), as well as certain information measures like S and E^O in the ground and a few low-lying states. Here, $k = 1$–4 represent dipole, quadrupole, octupole, and hexadecapole moments, respectively. In the GCHA model, the dependence of this degeneracy on principal (n) and orbital (ℓ) quantum numbers is analyzed. This helps us to find the exact number of degenerate states (in the GCHA) associated with a given FHA energy of the form $-\frac{Z^2}{2n^2}$. Further, we can also estimate the number of such degenerate states that exist in the GCHA. The calculation of dipole polarizability will guide us to examine the existence of the metallic character in excited states. To this end, pilot calculations are performed for ground and lower excited states by invoking the GPS method. This article is constructed as follows: Sec. II provides a brief description of the formalism employed in the present work. Section III offers a detailed discussion of the results. Finally, we conclude with a few remarks in Sec. IV.

II. THEORETICAL FORMALISM

The single-particle time-independent nonrelativistic radial SE for a spherically confined system is expressed (atomic units are employed unless otherwise stated) as

$$\left[-\frac{1}{2}\frac{d^2}{dr^2} + \frac{\ell(\ell+1)}{2r^2} + V_c(r)\right]\psi_{n,\ell}(r) = \mathcal{E}_{n,\ell}\ \psi_{n,\ell}(r), \quad (1)$$

where V_c represents the desired confined potential [3,39]:

$$V_c(r) = \begin{cases} v(r) & \text{for} \quad R_a \leqslant r \leqslant R_b, \\ \infty & \text{for} \quad 0 \leqslant r \leqslant R_a, \\ \infty & \text{for} \quad r \geqslant R_b. \end{cases} \quad (2)$$

Here, $v(r) = -\frac{Z}{r}$ signifies the electron-nuclear Coulomb attraction potential (Z refers to the nuclear charge). Throughout our work, $V_c(r)$ will be referred to as the GCHA. Depending upon the values of R_a and R_b, four distinct possibilities can be envisaged:

(i) The case with $R_a = 0$, $R_b = \infty$ gives rise to the FHA.

(ii) The case with $R_a = 0$, $R_b = r_c$, a finite number, corresponds to the CHA.

(iii) The case with $R_a \neq 0$, $R_b \neq \infty$, with R_a and R_b being finite, signifies the SCHA.

(iv) The case with $R_a \neq 0$, $R_b = \infty$ refers to the LCHA.

So that we could calculate the energy, spectroscopic properties, and information entropy, the GPS method was invoked. This provides a *nonuniform, optimal* spatial discretization that retains high accuracy at both small and large distances. In contrast to the standard finite-difference methods, a reasonably smaller number of grid point suffices, as this method facilitates a denser mesh at small r but a coarser mesh at large r. Further, by applying a *symmetrization* technique and a *nonlinear* mapping procedure, a *symmetric* eigenvalue equation is achieved. It is computationally orders of magnitude faster than finite-difference or finite-element methods. Thus, in essence, it combines the simplicity of a direct finite-difference or finite-element method with the fast convergence of finite-basis-set approaches. Over time, it has successfully been used to estimate various bound-state properties of several central potentials, including energy and other properties in CHAs and confined many-electron atoms [24,25,29,62–66].

A. Multipole polarizability

By definition, the static multipole polarizability can be conveniently written as

$$\alpha_i^{(k)} = \alpha_i^{(k)}(\text{bound}) + \alpha_i^{k}(\text{continuum}). \quad (3)$$

Conventionally $\alpha_i^{(k)}$ is expressed in terms of a compact sum-over-states form [67]. However, it can also be directly estimated by employing the standard perturbation-theory framework [68]. In the first procedure, Eq. (4) is modified to [69]

$$\begin{aligned}\alpha_i^{(k)} &= \sum_n \frac{f_{ni}^{(k)}}{(\mathcal{E}_n - \mathcal{E}_i)^2} \\ &\quad - c\int \frac{|\langle R_i|r^k Y_{kq}(\mathbf{r})|R_{\epsilon p}\rangle|^2}{(\mathcal{E}_{\epsilon p} - \mathcal{E}_i)}\, d\epsilon, \\ \alpha_i^{(k)}(\text{bound}) &= \sum_n \frac{f_{ni}^{(k)}}{(\Delta\mathcal{E}_{ni})2}, \\ \alpha_i^{k}(\text{continuum}) &= c\int \frac{|\langle R_i|r^k Y_{kq}(\mathbf{r})|R_{\epsilon p}\rangle|^2}{(\mathcal{E}_{\epsilon p} - \mathcal{E}_i)}\, d\epsilon. \end{aligned} \quad (4)$$

In Eq. (4), the summation and integral terms signify the bound and continuum contributions, respectively, $f_{ni}^{(k)}$ represents the multipole oscillator strength (k is a positive integer), and c is a *real* constant depending only on quantum number ℓ. q is an integer. Here, $f_{ni}^{(k)}$ measures the mean probability of transition between an initial state (i) and a final (n), which is normally expressed as

$$f_{ni}^{(k)} = \frac{8\pi}{(2k+1)}\Delta\mathcal{E}_{ni}|\langle r^k Y_{kq}(\mathbf{r})\rangle|^2. \quad (5)$$

Designating the initial and final states as $|n\ell m\rangle$ and $|n'\ell' m'\rangle$, we can easily derive

$$\begin{aligned} f_{ni}^{(k)} &= \frac{8\pi}{(2k+1)}\,\Delta\mathcal{E}_{ni}\,\frac{1}{2\ell+1}\sum_m \\ &\quad \times \sum_{m'} |\langle n'\ell' m'|r^k Y_{kq}(\mathbf{r})|n\ell m\rangle|^2. \end{aligned} \quad (6)$$

The application of the Wigner-Eckart theorem and sum rule for the *3j* symbol further leads to

$$f_{ni}^{(k)} = 2\,\frac{(2\ell'+1)}{(2k+1)}\,\Delta\mathcal{E}_{ni}|\langle r^k\rangle_{n\ell}^{n'\ell'}|^2 \begin{Bmatrix} \ell' & k & \ell \\ 0 & 0 & 0 \end{Bmatrix}^2. \quad (7)$$

The transition-matrix element is then given by the following radial integral:

$$\langle r^k\rangle = \int_0^\infty R_{n'\ell'}(r) r^k R_{n\ell}(r) r^2 dr. \quad (8)$$

Note that $f_{ni}^{(k)}$ depends on n and ℓ but is independent of the magnetic quantum number m. In this article, we compute $f^{(k)}$ and $\alpha^{(k)}$, with $k = 1$–4, for states with $\ell = 1$–4. It is necessary to point out that the following multipole oscillator-strength sum rule exists:

$$S^{(k)} = \sum_m f^{(k)} = k\langle\psi_i|r^{(2k-2)}|\psi_i\rangle, \quad (9)$$

where the summation includes all the bound and continuum states.

B. Information entropy

Information-entropic measures are functionals of density, and they quantify density in several complimentary ways. They have potential applications in atomic avoided crossing, the electron-correlation effect, quantum entanglement, the orbital-free density functional theory, etc. [25,29]. S is the arithmetic mean of uncertainty and is expressed as an expectation value of the logarithmic density. $S_{\mathbf{r}}$ measures the uncertainty in the localization of a particle in r space. A lower $S_{\mathbf{r}}$ indicates higher accuracy in predicting the localization. Similarly, $S_{\mathbf{p}}$ measures the uncertainty in predicting the momentum of a particle. $S_{\mathbf{r}}$ and $S_{\mathbf{p}}$ are expressed as

$$\begin{aligned} S_{\mathbf{r}} &= -\int_{\mathcal{R}^3} \rho(\mathbf{r})\ \ln[\rho(\mathbf{r})]\, d\mathbf{r} = 2\pi(S_r + S_{(\theta,\phi)}), \\ S_{\mathbf{p}} &= -\int_{\mathcal{R}^3} \Pi(\mathbf{p})\ \ln[\Pi(\mathbf{p})]\, d\mathbf{p} = 2\pi(S_p + S_{(\theta,\phi)}). \end{aligned} \quad (10)$$

Here, $\rho(\mathbf{r})$ and $\Pi(\mathbf{p})$ signify r- and p-space densities, both normalized to unity. Arguably, $S_{\mathbf{r}}$ and $S_{\mathbf{p}}$ provide the most appropriate uncertainty relation [70]. $S_{\mathbf{r}}$ and $S_{\mathbf{p}}$ are the logarithmic functionals of density. As a consequence, the total Shannon entropy is expressed as $S_{\mathbf{r}} + S_{\mathbf{p}}$,

$$S_t = S_{\mathbf{r}} + S_{\mathbf{p}} = 2\pi[S_r + S_p + 2S_{(\theta,\phi)}] \geqslant 3(1+\ln\pi). \quad (11)$$

The quantities S_r, S_p, and S_θ are defined as [70]

$$\begin{aligned} S_r &= -\int_0^\infty \rho(r)\ \ln[\rho(r)] r^2 dr, \\ S_p &= -\int_0^\infty \Pi(p) \ln[\Pi(p)]\ p^2 dp, \\ \rho(r) &= |\psi_{n,l}(r)|^2, \quad \Pi(p) = |\psi_{n,l}(p)|^2, \\ S_{(\theta,\phi)} &= -\int_0^\pi \chi(\theta)\ \ln[\chi(\theta)] \sin\theta d\theta, \quad \chi(\theta) = |\Theta(\theta)|^2. \end{aligned} \quad (12)$$

Another important measure studied in this work is E^O, referring to the second-order entropic moment [31]. It is the expectation value of density. It portrays behavior exactly opposite to S. It is also called disequilibrium, as it measures the deviation of a distribution from equilibrium [71]. In r and p space, the respective quantities are defined as

$$\begin{aligned} E_r^O &= \int_0^\infty [\rho(r)]^2 r^2 dr, \quad E_p^O = \int_0^\infty [\Pi(p)]^2 p^2 dp, \\ E_{\theta,\phi}^O &= \int_0^\pi [\chi(\theta)]^2 \sin\theta d\theta, \\ E_t^O &= E_r^O E_p^O [E_{\theta,\phi}^O]^2, \end{aligned} \quad (13)$$

where E_t^O is the total Onicescu information energy. Accurate r-space wave functions are obtained by applying the GPS

TABLE I. Incidental degeneracy in the GCHA associated with $n = 4$ for the FHA. See the text for details.

Serial	No. of nodes	State	R_a	R_b	Energy	FHA	$\alpha^{(1)}$	$S_{\mathbf{r}}$
a	0	$1s$	0	1.87164450	−0.03125000	$4s$	0.27404101	2.22927677
b	0	$1s$	1.87164450	6.6108150	−0.03125000	$4s$	169.7527968	6.55734580
c	0	$1s$	6.6108150	15.51755	−0.03125000	$4s$	8609.5280939	9.15073565
d	0	$1s$	15.51755	100	−0.03125000	$4s$	322925.0793	12.14484806
e	1	$2s$	0	6.6108150	−0.03125000	$4s$	−128.96450306	6.35223141
f	1	$2s$	1.87164450	15.51755	−0.03125000	$4s$	2265.40684074	9.10240049
g	1	$2s$	6.6108150	100	−0.03125000	$4s$	173868.83409	12.14272018
h	2	$3s$	0	15.51755	−0.03125000	$4s$	129.09470914	9.01151759
i	2	$3s$	1.87164450	100	−0.03125000	$4s$	80408.86663	12.09689745
j	3	$4s$	0	100	−0.03125000	$4s$	4992.00000000	12.07490387
k	0	$2p$	0	10-2$\sqrt{5}$	−0.03125000	$4p$	13.56524044	5.42877070
l	0	$2p$	10-2$\sqrt{5}$	10+2$\sqrt{5}$	−0.03125000	$4p$	1711.37938497	8.51079967
m	0	$2p$	10-2$\sqrt{5}$	125	−0.03125000	$4p$	84939.073612	11.63160747
n	1	$3p$	0	10+2$\sqrt{5}$	−0.03125000	$4p$	−977.65896463	8.32046807
o	1	$3p$	10-2$\sqrt{5}$	105	−0.03125000	$4p$	40632.47423	11.61219021
p	2	$4p$	0	125	−0.03125000	$4p$	5107.1999999	11.53386387
q	0	$3d$	0	12	−0.03125000	$4d$	203.03802379	7.82189131
r	0	$3d$	12	120	−0.03125000	$4d$	18.72296856	11.37785020
s	1	$4d$	0	125	−0.03125000	$4d$	5760.000000	11.26209911
t	2	$4f$	0	130	−0.03125000	$4f$	6720.000000	10.86085521

method. The corresponding p-space wave function is generated by Fourier transforming its r-space counterpart. This is accomplished quite efficiently by following the procedure adopted in [25].

III. RESULTS AND DISCUSSION

In [39], all three models (CHA, SCHA, LCHA) were mentioned under the general SCHA heading. However, since they have quite different energy characteristics, we discuss them separately here. The demonstrative results are presented for only H atoms ($Z = 1$). However, a similar outcome can also be extracted for $Z \neq 1$ cases. Thus, first, we shall analyze the salient features of incidental degeneracy achieved by placing the boundary at respective nodal positions of a FHA. Then we present $f^{(k)}(Z)$ and $\alpha^{(k)}(Z)$ ($k = 1$–4) for selected low-lying states in these four potentials. Further, in the realm of the Herzfeld criterion of metallic behavior, we have computed $\alpha^{(1)}(Z)$ for the $1s, 2s, 2p, 3d, 4f$, and $5g$ states. As a bonus, analytical closed-form expressions of $f^{(k)}(Z)$ and $\alpha^{(k)}(Z)$ are derived for all six states. Finally, we consider $S_{\mathbf{r}}, S_{\mathbf{p}}, S$ as well as $E^{O}_{\mathbf{r}}, E^{O}_{\mathbf{p}}, E$ in the ground state involving these four potentials. It is worth mentioning that, in the case of degeneracy, radial boundaries are chosen specifically at the nodes of the FHA to illustrate their role. However, for other properties ($f^{(k)}, \alpha^{(k)}$, information entropy), no such factor was taken into consideration. Thus, they are selected to illustrate the essential features related to an individual property.

A. Incidental degeneracy

Following [39], it may happen that the energy of a given confined state becomes equal to that of an unconfined state (here, it is $-\frac{Z}{2n^2}$) when the radius of confinement is suitably chosen at the location of radial nodes in latter state. Such a phenomenon is termed *incidental degeneracy*. Equation (2) showed that the *shell-confined* condition renders four different systems. This degeneracy may provide a connection among them.

1. H-like ion

It is known that, if R_a and R_b of a GCHA coincide with certain specific radial nodes of the (n, ℓ) state of a FHA, then $(n' - \ell - 1)$ nodes exist between them. Furthermore, the energy of such an (n', ℓ) GCHA state becomes degenerate to that of a FHA state. First, we wish to determine the *number of degenerate states* associated with a given FHA energy, $-\frac{Z^2}{2n^2}$. It is worth mentioning that in this part we shall discuss only the states that arise as a result of placing the boundary at nodal points of the FHA. For demonstrative purposes, we present all 10 states belonging to $n \leqslant 4$ of the GCHA in Table I. The corresponding boundaries are chosen from radial nodes of $4s, 4p, 4d$ states of the FHA. Thus, as can be seen, a total of 20 degenerate states exist in the GCHA, all having the same energy of −0.031250 a.u., corresponding to $n = 4$ of the FHA. Out of that, the numbers of s, p, d, and f states are 10, 6, 3, and 1, respectively. It is also recognized that there are 6 (a, e, h, k, n, q), 4 (b, c, f, l), 6 (d, g, i, m, o, r), and 4 (j, p, s, t) states belonging to the CHA, SCHA, LCHA, and FHA, respectively. The last two columns tabulate the respective $\alpha^{(1)}$ $(\Delta\ell = 1)$ and S_r. One can see that in the SCHA $\alpha^{(1)}$ has a higher value compared to those in the CHA and FHA counterparts.

It is well known that, in the FHA, the energies of all the ℓ states (0 to $n - 1$) within a given n are the same. Now, from an observation of the results in Table I, it can be seen that $\frac{(n-\ell)(n-\ell+1)}{2}$ isoenergic states appear in the GCHA. Thus, for a given n state of a FHA, the total number of degenerate GCHA states works out to be

$$\frac{1}{2}\sum_{\ell=0}^{(n-1)}(n-\ell)(n-\ell+1) = \frac{1}{2}\sum_{\ell=0}^{(n-1)}(n-\ell)^2 + \sum_{\ell=0}^{n-1}(n-\ell) = \frac{n(n+1)}{2} + \frac{n(n+1)(2n+1)}{12} = \frac{n(n+1)(n+2)}{6}. \tag{14}$$

This result suggests that the number *does not* depend on ℓ. Now, we can determine the contribution of each of these four categories in this degeneracy as follows.

(i) *FHA*. For a particular n, n degenerate states exist.

(ii) *CHA*. In this case, an ℓ orbital contributes $(n-\ell-1)$ degenerate states. Thus, the total number of degenerate states is then given by

$$\sum_{\ell=0}^{(n-1)}(n-\ell-1) = \frac{n(n-1)}{2}. \tag{15}$$

(iii) *SCHA*. In the s orbital, the first SCHA state occurs with energy equal to $n=3$ of the FHA [39]. Similarly, for the p orbital, it has energy equal to $n=4$ of the FHA. So for a given ℓ, the first degenerate SCHA state appears at $n=(\ell+3)$ with energy $-\frac{z^2}{2(\ell+3)^2}$. For a given n, such states can be achieved up to $\ell = (\ell_{\max}-2) = (n-3)$. Therefore, at a fixed n, a given ℓ state contributes as $\frac{(n-\ell-2)(n-\ell-1)}{2}$, giving the total number as

$$\sum_{\ell=0}^{(n-3)}\frac{(n-\ell-2)(n-\ell-1)}{2} = \frac{n(n-1)(n-2)}{6} \tag{16}$$

(iv) *LCHA*. Similar to the CHA, here also, a particular ℓ orbital will contribute $(n-\ell-1)$ degenerate states, giving the same total as in the CHA, namely, $\sum_{\ell=0}^{(n-1)}(n-\ell-1) = \frac{n(n-1)}{2}$.

Next, we estimate the individual contribution of all four systems in the above degeneracy. On the basis of the above discussion and following Table I, we can find certain characteristics. To facilitate this, we use n and ℓ to denote principal and orbital quantum numbers of the FHA, whereas n_k and ℓ_j signify the same for the other three systems (k, j are integers).

(i) Corresponding to the nth state of the FHA, there are $\frac{n(n+1)(n+2)}{6}$ degenerate GCHA states, each having the same energy $-\frac{Z^2}{2n^2}$.

(ii) Each ℓ state belonging to a certain n contributes $\frac{(n-\ell)(n-\ell+1)}{2}$ GCHA states.

(iii) The number of incidental degenerate states increases with n. However, at a fixed n, the number of such states reduces with a rise in ℓ.

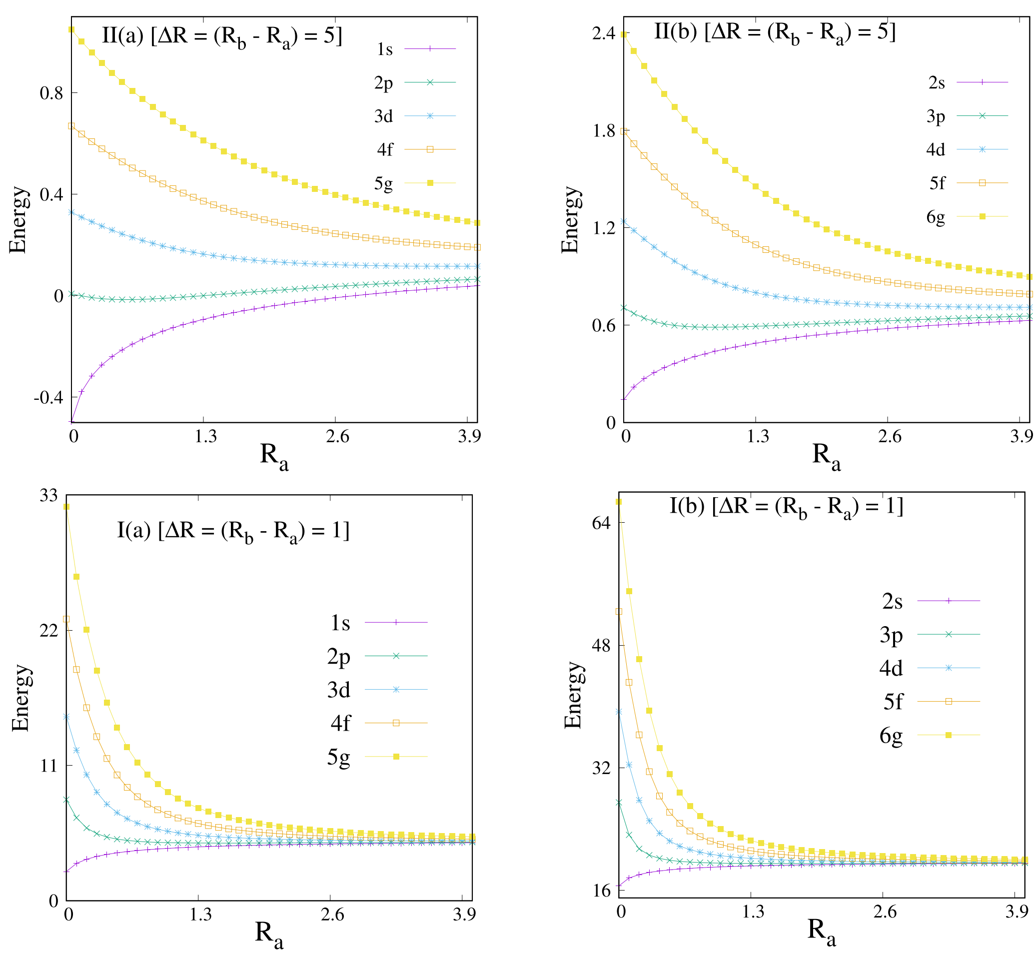

FIG. 1. Energy as a function of R_a (in a.u.) in the SCHA for (I) $\Delta R = (R_b - R_a) = 1$ and (II) $\Delta R = (R_b - R_a) = 5$ for (a) circular and (b) single-node states. See text for details.

TABLE II. Incidental degeneracy in WCP and the ECSCP for $\lambda_1, \lambda_2 = 0.01$ a.u. See the text for details.

Serial	No. of nodes	State	R_a	R_b	Energy	Free state	$\alpha^{(1)}$	$S_{\mathbf{r}}$
				WCP				
2*a*	0	1*s*	0	2.000390	−0.115293282	2*s*	0.34278641	2.39716825
2*b*	0	1*s*	2.000390	100	−0.115293282	2*s*	932.14066065	8.21415856
2*c*	1	2*s*	0	100	−0.115293282	2*s*	120.5848668	8.11443243
3*a*	0	1*s*	0	1.902698	−0.046198857	3*s*	0.28975431	2.27113719
3*b*	0	1*s*	1.902698	7.108762	−0.046198857	3*s*	208.23885866	6.75134003
3*c*	0	1*s*	7.108762	150	−0.046198857	3*s*	28579.047941	10.53960365
3*d*	1	2*s*	0	7.108762	−0.046198857	3*s*	−207.14861496	6.56892996
3*e*	1	2*s*	1.9026980	150	−0.046198857	3*s*	12624.6506	10.48406780
3*f*	2	3*s*	0	150	−0.046198857	3*s*	1033.70055187	10.44196440
4*a*	0	1*s*	0	1.8729343	−0.022356120	4*s*	0.27468622	2.23104252
4*b*	0	1*s*	1.8729343	6.6268050	−0.022356120	4*s*	170.96931921	6.56397087
4*c*	0	1*s*	6.6258050	15.6046240	−0.022356120	4*s*	8757.380222	9.16720124
4*d*	0	1*s*	15.6046240	150	−0.022356120	4*s*	337593.5180	12.18838925
4*e*	1	2*s*	0	6.6268050	−0.022356120	4*s*	−131.07497378	6.35963966
4*f*	1	2*s*	1.8729343	15.6046240	−0.022356120	4*s*	2309.54693312	9.11891006
4*g*	1	2*s*	6.6268050	150.0	−0.022356120	4*s*	182824.8322	12.18544076
4*h*	2	3*s*	0	15.6046240	−0.022356120	4*s*	131.30125522	9.02899807
4*i*	2	3*s*	1.8729343	150	−0.022356120	4*s*	85268.9345	12.14058812
4*j*	3	4*s*	0	150	−0.022356120	4*s*	5294.641728	12.11924015
				ECSCP				
2*a*	0	1*s*	0	2.0000208	−0.115013458	2*s*	0.34257005	2.39669558
2*b*	0	1*s*	2.0000208	100	−0.115013458	2*s*	928.75702501	8.21114396
2*c*	1	2*s*	0	100	−0.115013458	2*s*	120.07106878	8.11127833
3*a*	0	1*s*	0	1.90200530	−0.045619079	3*s*	0.28939390	2.27020331
3*b*	0	1*s*	1.90200530	7.0994429	−0.045619079	3*s*	207.43129440	6.74776731
3*c*	0	1*s*	7.0994429	150	−0.045619079	3*s*	28215.90613	10.52774639
3*d*	1	2*s*	0	7.0994429	−0.045619079	3*s*	−205.22594788	6.56497789
3*e*	1	2*s*	1.902000530	150	−0.045619079	3*s*	12430.91176	10.47209351
3*f*	2	3*s*	0	150	−0.045619079	3*s*	1017.71439735	10.42967937
4*a*	0	1*s*	0	1.87185526	−0.021437465	4*s*	0.27414583	2.22956395
4*b*	0	1*s*	1.87185526	6.61372660	−0.021437465	4*s*	169.96865645	6.55854163
4*c*	0	1*s*	6.61372660	15.5362170	−0.021437465	4*s*	8639.641193	9.15424609
4*d*	0	1*s*	15.5362170	150	−0.021437465	4*s*	327409.3061	12.15969133
4*e*	1	2*s*	0	6.61372660	−0.021437465	4*s*	−129.33805232	6.35357332
4*f*	1	2*s*	1.87185526	15.5362170	−0.021437465	4*s*	2274.9433235	9.10593888
4*g*	1	2*s*	6.61372660	150.0	−0.021437465	4*s*	176835.0570	12.15740646
4*h*	2	3*s*	0	15.6046240	−0.021437465	4*s*	129.58544973	9.02879432
4*i*	2	3*s*	1.87185526	150	−0.021437465	4*s*	82114.5084	12.11197447
4*j*	3	4*s*	0	150	−0.021437465	4*s*	5112.60426	12.09022342

(iv) The first occurrence of the degenerate SCHA state takes place at $n = 3$.

(v) At a fixed ℓ, $n_1 < n$. This suggests that n_1 takes values from $(\ell + 1)$ to $n - 1$. If we choose $n = 4$, then $\mathcal{E}_4 = -0.03125$. Therefore, for $\ell = 0$, $n_1 = 1, 2, 3$; for $\ell = 1$, $n_1 = 2, 3$; and when $\ell = 2$, $n_1 = 3$.

(vi) Two arbitrary states (n_1, ℓ_1) and (n_2, ℓ_2) are degenerate when $n_1 < n, \ell_1 < n$ and $n_2 < n, \ell_2 < n$. Note that they may belong to any of the systems in GCHA, except the FHA.

When both R_a and R_b are finite and nonzero (i.e., the SCHA), the behavior of the particle is deeply influenced by R_a, R_b, and $\Delta R = (R_b - R_a)$. However, controlling any two parameters would also serve the purpose of the remaining one. It is found that at a fixed R_b, the energy of a given state progresses with R_a (smaller ΔR). Conversely, at a given R_a, a reverse pattern is noticed with a rise in R_b (larger ΔR). It is of interest to monitor the energy pattern for a fixed ΔR, with modulations in both R_a and R_b, which is depicted in Fig. 1. The bottom and top panels display energy as a function of R_a at two selected ΔR, namely, 1 (panel I) and 5 (panel II). Figures 1(a) and 1(b) record the first five circular ($1s, 2p, 3d, 4f, 5g$) and single-node ($2s, 3p, 4d, 5f, 6g$) states, respectively. A careful observation reveals that, in either case, the energy of $\ell = 0$ states ($1s, 2s$) gradually rises with R_a (squeezing of the box). In contrast, $\ell \neq 0$ states record a decay in the energy with growth in R_a, initially at a quick pace and then slowing down until becoming flat at sufficiently large R_a. However, for $\ell > 0$, there is harmony among the states with slight differences in the lower R_a region.

TABLE III. $f^{(1)}$ values for the $1s$, $2s$, $2p$ states in the CHA, SCHA, and LCHA. See the text for details.

R_a	R_b	$1s \rightarrow 2p$	$1s \rightarrow 3p$	$2s \rightarrow 2p$	$2s \rightarrow 3p$	$2p \rightarrow 1s$	$2p \rightarrow 2s$	$2p \rightarrow 3d$	$2p \rightarrow 4d$
0	1	0.98455839	0.00772592	−0.60825789	1.56032656	−0.32818613	0.20275263	1.08482483	0.01857681
0.1	1	0.89910222	0.09117798	−0.54875155	1.26759877	−0.29970074	0.18291718	1.07826147	0.02579334
0.2	1	0.81158829	0.17664462	−0.46434643	1.01215223	−0.27052943	0.15478214	1.04448022	0.05966553
0.5	1	0.69746119	0.28964404	−0.35084205	0.73447901	−0.23248706	0.11694735	0.92955029	0.17316032
0.8	1	0.66991458	0.31699958	−0.32345071	0.67370461	−0.22330486	0.10781690	0.89321899	0.20918396
0	2	0.99105877	0.00000217	−0.61189926	1.57832558	−0.33035292	0.20396642	1.09062730	0.01308847
0.1	2	0.96414685	0.02875100	−0.60923016	1.46958646	−0.32138228	0.20307672	1.08969744	0.01424386
0.5	2	0.78114997	0.20643653	−0.43425912	0.93184418	−0.26038332	0.14475304	1.02245081	0.08147398
1	2	0.69749557	0.28958819	−0.35086313	0.73452648	−0.23249852	0.11695438	0.92959980	0.17310450
1.2	2	0.68355578	0.30344579	−0.33700278	0.70354791	−0.22785193	0.11233426	0.91134321	0.19119914
1.5	2	0.67205870	0.31486957	−0.32557999	0.67836486	−0.22401957	0.10852666	0.89607618	0.20634732
1.8	2	0.66739177	0.31950490	−0.32094504	0.66823564	−0.22246392	0.10698168	0.88985569	0.21252327
0	5	0.84879929	0.10827497	−0.45637469	1.42333674	−0.28293310	0.15212490	1.10303346	0.00102259
1	5	0.82132944	0.16452278	−0.47393100	1.02743235	−0.27377648	0.15797700	1.05560747	0.04906997
2	5	0.72015051	0.20643653	−0.37324792	0.78555850	−0.24005017	0.12441597	0.95825952	0.14467096
2.5	5	0.69759377	0.28958819	−0.35089758	0.73466209	−0.23253126	0.11696586	0.92974209	0.17292899
3	5	0.68357365	0.30344579	−0.33700060	0.70357230	−0.22785788	0.11233353	0.91136832	0.19116227
4	5	0.66991478	0.31486957	−0.32344989	0.67370488	−0.22330493	0.10781663	0.89321926	0.20918302
4.5	5	0.66739177	0.31950490	−0.32094500	0.66823564	−0.22246392	0.10698167	0.88985569	0.21252323
0	10	0.49203980	0.25817376	−0.07781857	0.96754959	−0.16401327	0.02593952	1.07006404	0.02801599
0.5	10	0.97045316	0.01437069	−0.62098640	1.56331874	−0.32348439	0.20699547	1.08623978	0.01685871
1	10	0.94767400	0.02402487	−0.58992446	1.36743381	−0.31589133	0.19664149	1.10659524	0.00041483
2	10	0.82883015	0.14973954	−0.47587757	1.03956806	−0.27627672	0.15862586	1.06686692	0.03701308
3	10	0.75955649	0.22459445	−0.41041279	0.87499038	−0.25318550	0.13680426	1.00438637	0.09839538
5	10	0.69774060	0.28903455	−0.35085740	0.73486495	−0.23258020	0.11695247	0.92995783	0.17260954
7	10	0.67494769	0.31198282	−0.32843445	0.68465713	−0.22498256	0.10947815	0.89992293	0.20251950
9.5	10	0.66683858	0.32005426	−0.32039568	0.66703853	−0.22227953	0.10679856	0.88911811	0.21325570
0	∞	0.41619672	0.07910156	0.00000000	0.43486544	−0.13873224	0.00000000	0.69578470	0.12179511
0.1	∞	0.61261825	0.08716313	−0.27197479	0.76653089	−0.20420608	0.09065826	0.69643208	0.12177348
0.5	∞	0.91228737	0.03992888	−0.50501203	1.34020061	−0.30409579	0.16833734	0.73703538	0.11966976
1	∞	0.95710827	0.00509331	−0.46634518	1.42628570	−0.31903609	0.15544839	0.84505124	0.10660158
2	∞	0.91518127	0.00537086	−0.38224386	1.32047405	−0.30506042	0.12741462	1.01517164	0.05572610
5	∞	0.82683246	0.05128960	−0.29816602	1.10002016	−0.27561082	0.09938867	1.08031802	0.00001907
7	∞	0.79907239	0.07217889	−0.27883906	1.02880135	−0.26635746	0.09294635	1.05975869	0.00511577
8	∞	0.78916499	0.08038843	−0.27256657	1.00309177	−0.26305500	0.09085552	1.04975557	0.00959527
9	∞	0.78094995	0.08751295	−0.26761185	0.98164753	−0.26031665	0.08920395	1.04067662	0.01429067
10	∞	0.77400929	0.09376540	−0.26360162	0.96343656	−0.25800310	0.08786721	1.03254711	0.01891643

2. H plasma

Now, an important question arises: is this special degeneracy a unique feature of one-electron Coulombic systems? To examine it, we extend the calculations to two familiar plasma models: (i) weakly coupled plasma (WCP) or Debye plasma, governed by a potential, $V(r) = -\frac{Z}{r}e^{-\lambda_1 r}$, and (ii) the exponential-cosine-screened Coulomb potential (ECSCP), given by $V(r) = -\frac{Z}{r}e^{-\lambda_2 r}\cos\lambda_2 r$. Here, λ_i is the inverse of the Debye radius and represents the interaction between the electron and ions in a plasma [72]. In particular, $\lambda_1 = \sqrt{\frac{4\pi e^2 n_e}{k_b T}}$ (n_e, k_b, and T stand for ion density, Boltzmann's constant, and plasma temperature, respectively), while $\lambda_2 = \frac{k_q}{\sqrt{2}} = \sqrt{\frac{n_e \omega_{pe}}{\hbar}}$ (k_q is the electron plasma wave number related to the plasma frequency and number density). Note that, in WCP, classical interactions are considered, while the quantum effect in a plasma can be added by invoking a $\cos\lambda r$ term in WCP [73]. These two prototypical systems have been studied heavily, offering a vast literature. Thus, the influence of screening on the energy spectrum [72,74–76], the photoionization cross section [77–79], and electron-impact excitations [80,81] has been investigated with great interest. Generally speaking, plasma systems have a finite number of bound states, which decreases with the enhancement of λ.

Let us recall that, in contrast to a FHA, the plasma models, WCP and ECSCP, are *devoid* of accidental degeneracy. Table II illustrates the incidental degeneracy for these models, with $n = 2$–4 in s (or $\ell = 0$) states. Like in the GCHA, here also, R_a and R_b are placed at the nodal positions of respective s states in *free* plasmas. In WCP, at $n = 2$ (energy $= -0.1152930$ a.u.), a threefold degeneracy exists with one confined ($2a$), one left-confined ($2b$), and one

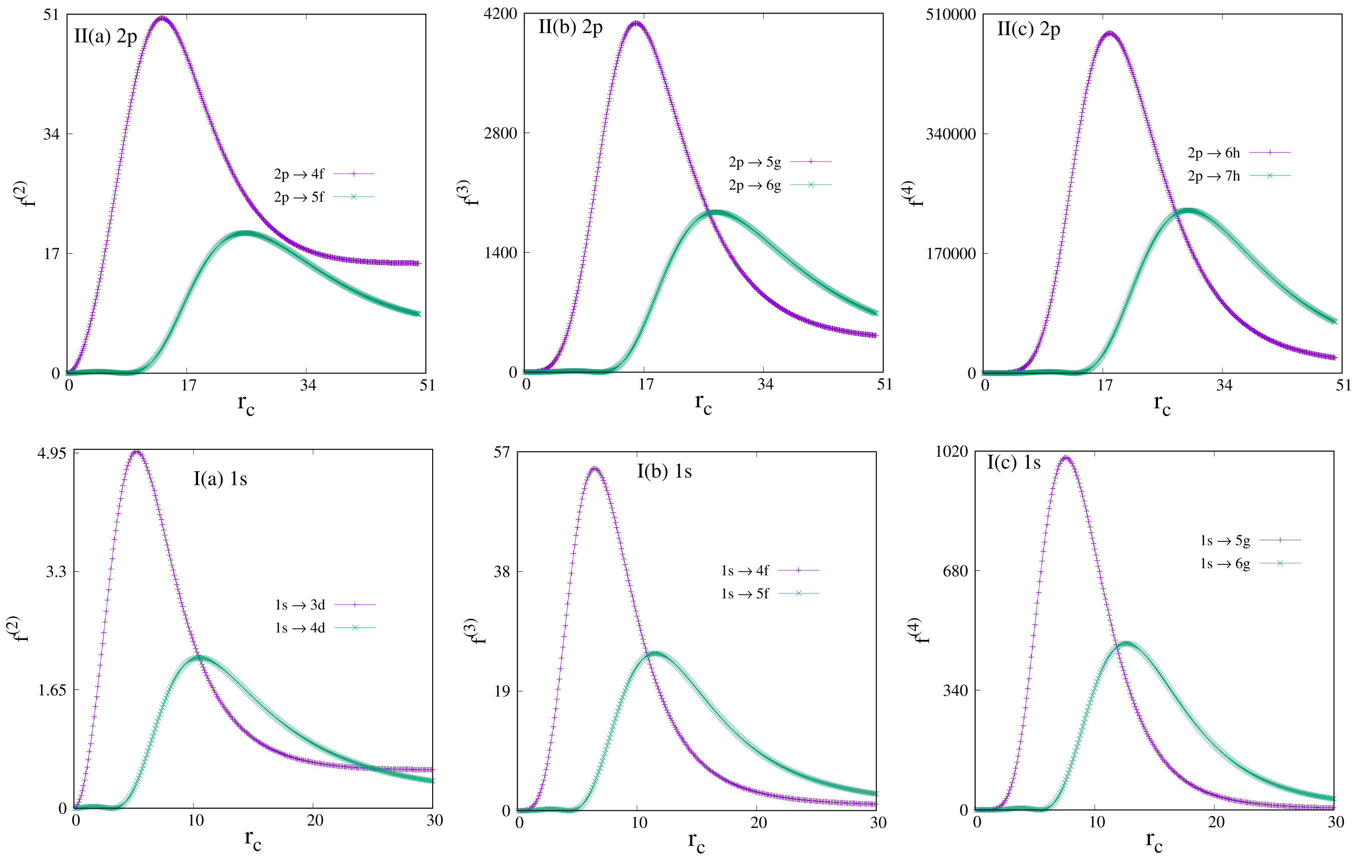

FIG. 2. Plot of $f^{(k)}$ as a function of r_c (in a.u.) for (I) $1s$ and (II) $2p$ states in the CHA. The first two transitions are shown; (a), (b), and (c) have $k = 2, 3, 4$, respectively. See the text for details.

free ($2c$) WCPs. This degeneracy in the *shell-confined* WCP, however, arises at $n = 3$ at an energy of -0.04619881 a.u. Thus, at $n = 3$, six degenerate states survive in the *generalized confined* WCP, namely, confined ($3a, 3d$), shell-confined ($3b$), left-confined ($3c, 3e$), and free ($3f$) WCPs. Further, at $n = 4$ (energy $= -0.0223561$ a.u.), there are 10 degenerate states belonging to confined ($4a, 4e, 4h$), shell-confined ($4b, 4c, 4f$), left-confined ($4d, 4g, 4i$), and free ($4j$) WCPs, respectively. Moving to the ECSCP system, we encounter a pattern of degeneracy exactly identical to that in WCP, with obvious energy differences between the two. This amply displays the existence of incidental degeneracy in these two plasma systems, implying that such a degeneracy is not necessarily limited to FHAs and may occur in other quantum systems as well. The last two columns in Table II show $\alpha^{(1)}$ and S_r. It may be mentioned here that WCP and ECSCP were invoked to establish the existence of incidental degeneracy in plasma potentials. We have not gone beyond this point to undertake an elaborate study of incidental degeneracy in these two or other systems, and that may be explored in the future.

B. Multipole oscillator strength and polarizability

Unlike in the previous section on energy, here, we split the discussion of $f^{(k)}$ and $\alpha^{(k)} (k = 1 - 4)$ in confined H-like ions and their *free* counterpart in some low-lying states. Except for $\alpha^{(1)}$ of $1s$ in a SCHA, no such results have been reported so far for any of the other GCHA models. Wherever possible, our results are compared with the available literature. As an offshoot, analytical closed-form expressions for $f^{(k)}$ and $\alpha^{(k)}$ (considering the bound-state contribution) are presented in the Appendix for $k = 1, 2, 3, 4$ in the case of a FHA.

At the outset, we note that the oscillator-strength sum rule, Eq. (9), is verified for all states in the CHA, SCHA, and LCHA for $k =$ 1–4. By definition, $f^{(k)}$ determines the probability of a transition from an initial to a final state. For absorption and emission it is positive and negative respectively.

The selection rule for $f^{(1)}$ is $\Delta\ell = \pm 1$. Note that, from an s state, only a transition to a p state can take place. However, from p, a transition can be to both s and d states. Table III gives the calculated $f^{(1)}$ for $1s, 2s, 2p$ for $n, \ell \rightarrow n', (\ell + 1)$ ($n = 1, 2; n' = 2, 3, 4$) transitions. In this context, SCHA results are offered for four R_b, namely, 1,2,5,10; for each R_b, R_a lies between zero and R_b. The bottom part shows results for the LCHA, which has 10 separate R_a (including 0, leading to the special case of the FHA), for $R_b = \infty$. Further, one recovers a CHA situation when $R_a = 0$, while $r_c = R_b = 1, 2, 5, 10$. It is noticed that $f^{(1)}_{1s\rightarrow 2p}$ in the CHA increases with r_c to attain a maximum and then falls to merge to the FHA. In the SCHA, for $R_b \leqslant 5$, it decreases with a rise in R_a, but at $R_b = 10$, it slowly reaches a maximum before finally decreasing. In contrast, in the LCHA, it grows with R_a to attain a maximum and then decays. The behavior of $f^{(1)}_{1s\rightarrow 3p}$

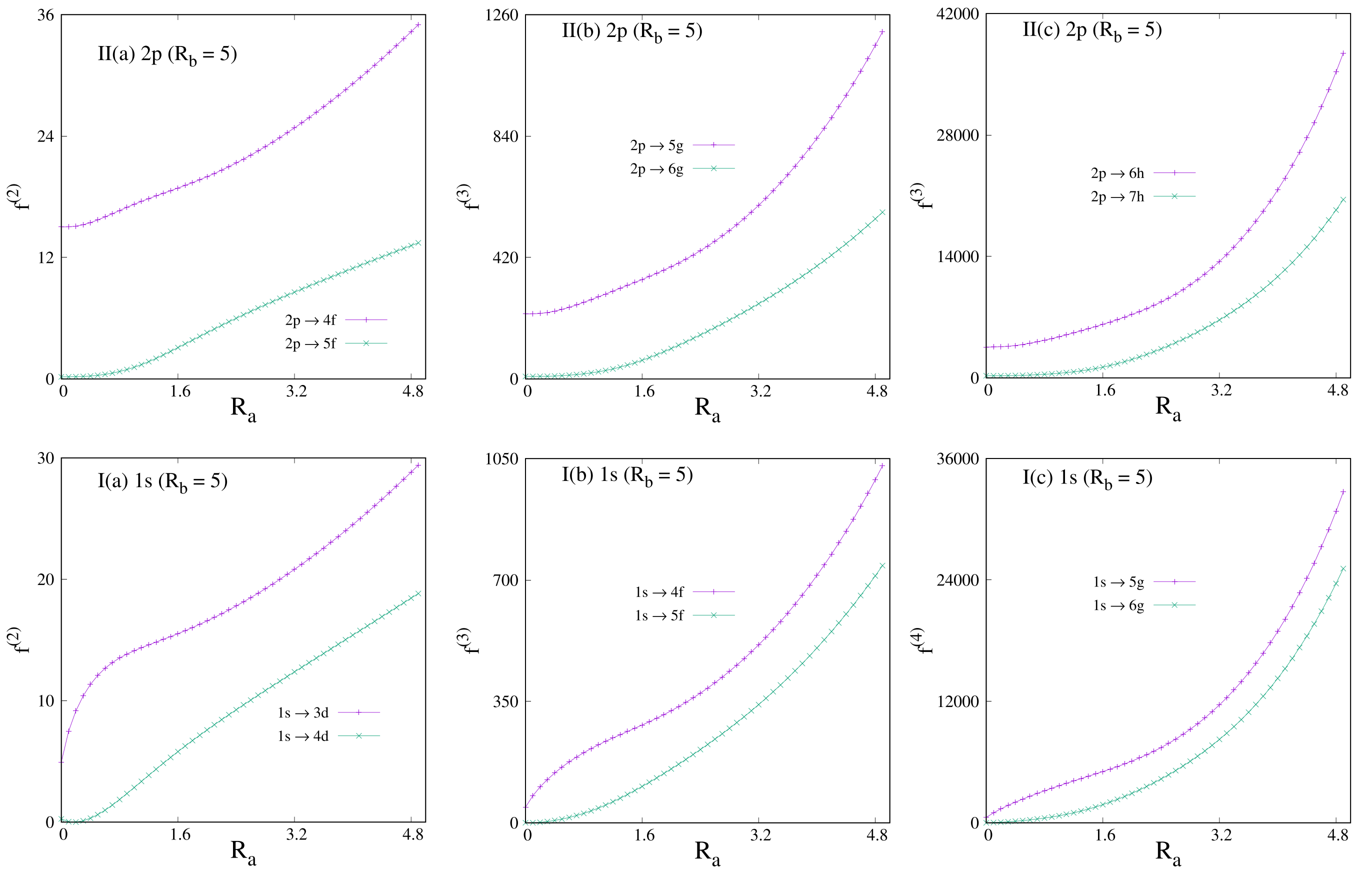

FIG. 3. Plot of $f^{(k)}$ as a function of R_a (in a.u.), keeping R_b fixed at 5, for (I) $1s$ and (II) $2p$ states in the SCHA. The first two transitions are shown; (a), (b), and (c) have $k = 2, 3, 4$, respectively. See the text for details.

is, however, somehow different from $f^{(1)}_{1s\to 2p}$; for example, a reverse trend is recorded in the case of the CHA. However, at $r_c \to \infty$, eventually, it converges to the FHA. In the SCHA, the pattern generated for a given R_b for various R_a generally differs with a change in R_b. However, in the LCHA it travels through a maximum and then a minimum and again increase. In the case of the $2s \to 2p$ transition, $f^{(1)}$ is always (−)ve, which implies that, except in the FHA (where they are degenerate), the former has higher energy than latter. As usual, in the CHA $f^{(1)}_{2s\to 2p}$ approaches the FHA limit for $R_a \to 0$, $R_b \to \infty$. In the SCHA, at $R_b = 1$ (and 2), it increases with R_a, but for $R_b = 5$ (and 10), it reaches a minimum and then increases. A similar pattern is also noticed in the LCHA for $R_b = 5$ (and 10). In the case of the $2s \to 3p$ transition, $f^{(1)}$ in the CHA and LCHA imprint resembling nature, i.e., decay after attaining a maximum. But the trend in the SCHA differs from $R_b \leqslant 5$ (it decreases as R_a progresses). At $R_b = 10$, a reverse trend is recorded. In contrast to $1s$ and $2s$, the behavior of $f^{(1)}$ in $2p$ is not straightforward. Nevertheless, a few comments can be made: (i) at the $r_c \to \infty$ limit, the CHA results converge to the FHA, (ii) $f^{(1)}$ in the SCHA (at $R_b = 10$) and the LCHA display analogous characters, although in particular cases this pattern alters, and (iii) $f^{(1)}_{2p\to 3d}$ and $f^{(1)}_{2p\to 4d}$ have opposite features.

Now, the focus is on higher-order $f^{(k)}$, for which results are depicted graphically for the cases of $k = 2$–4, related to *quadrupole, octupole, and hexadecapole* transitions. The corresponding selection rules are $\Delta\ell = 0, \pm 2$, $\Delta\ell = \pm 1, \pm 3$, and $\Delta\ell = 0 \pm 2, \pm 4$, respectively. In Fig. 2, the bottom and top rows represent transitions from the $1s$ and $2p$ states for the respective maximum $\Delta\ell$ values, with $k = 2, 3, 4$ in Figs. 2(a), 2(b) and 2(c), respectively. For each k, the first two transitions from these two states are exhibited in terms of $f^{(k)}$ versus r_c in the CHA. In the case of the $1s \to (3d, 4f, 5g)$ and $2p \to (4f, 5g, 6h)$ transitions, respective $f^{(k)}$ pass through a distinct maximum. But for the remaining six transitions, *viz.*, $1s \to (4d, 5f, 6g)$ and $2p \to (5f, 6g, 7h)$, a shallow maximum appears, followed by a prominent one. Figure 3 exhibits the variation of $f^{(2)}$, $f^{(3)}$, and $f^{(4)}$ in the left, middle, and right panels, respectively, as a function of R_a in the SCHA, keeping R_b stationary at 5. The same two states generating the same transitions as in Table III are considered. In this instance, $f^{(k)}$ always advances with R_a. Figure 4 plots $f^{(k)}$ against R_a, keeping $\Delta R = (R_b - R_a)$ fixed at 1, in the SCHA. The presentation strategy is similar to that in Figs. 2 and 3. In all cases, $f^{(k)}$ progress with R_a. Likewise, Figs. 5(a)–5(c) depict $f^{(2)}$ for $1s \to 3d$, $2p \to 4f$; $f^{(3)}$ for $1s \to 4f$, $2p \to 5g$; and $f^{(3)}$ for $1s \to 5g$, $2p \to 6h$ transitions in the LCHA, respectively. We find that, like in Fig. 4, here also, $f^{(k)}$ grow with R_a; the y axis dramatically increases as k goes from 2 to 4.

Now we move to investigate $\alpha^{(1)}$ in the GCHA by means of sample calculations for $1s, 2s, 2p, 3s, 3d, 4s$ states. For the p

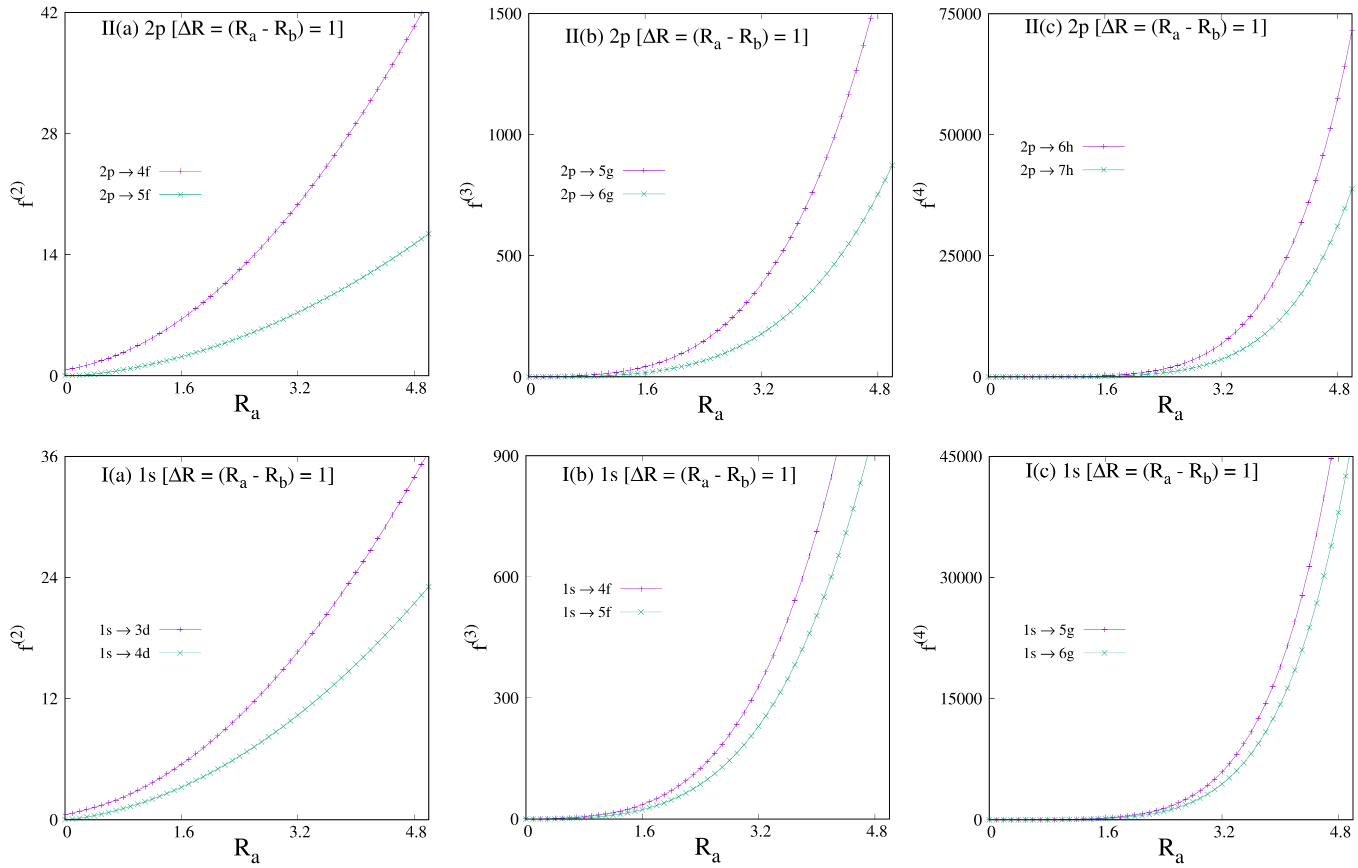

FIG. 4. Plot of $f^{(k)}$ (in a.u.) as a function of R_a for $\Delta R = (R_b - R_a) = 1$ in (I) $1s$ and (II) $2p$ states in the SCHA. First two transitions are shown; (a), (b), and (c) have $k = 2, 3, 4$, respectively. See the text for details.

and d states, allowed transitions occur in final states with ℓ of (0,2) and (1,3), respectively. The results collected in Table IV include contributions from both ℓ for the same numerical values of R_a and R_b as in Table III. The third column provides the volume of a ring ($V = R_b^3 - R_a^3$) with inner and outer radii R_a and R_b. Note that $(R_a, R_b) = (0, 1), (0, 2), (0, 5), (0, 10)$ represent CHA cases. The LCHA results are tabulated at the bottom, while the first row corresponds to a FHA. Some of the results for the CHA and SCHA were reported in [3] and are duly quoted in the footnotes. Our calculated $\alpha^{(1)}$ values show excellent agreement with these results. A careful analysis of Table IV uncovers several interesting features, some of which are as follows:

(i) *CHA*. In a FHA, $\alpha^{(1)}$ is a (+)ve quantity. At a given ℓ, it increases in n, while at a fixed n, it progresses with ℓ. However, in the CHA, the pattern behavior is not as consistent,

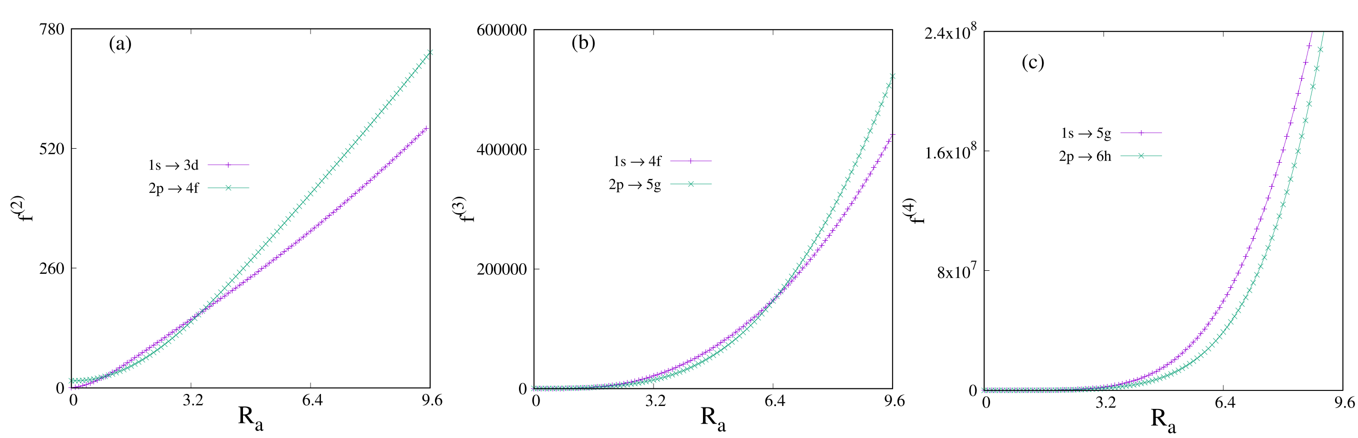

FIG. 5. Plot of $f^{(k)}$ (in a.u.) as a function of R_a for $1s$ and $2p$ states in the LCHA. (a), (b), and (c) have $k = 2, 3, 4$, respectively. See the text for details.

TABLE IV. $\alpha^{(1)}$ values for the $1s$, $2s$, $3s$, $4s$, $2p$, $3d$ states in the GCHA. See the text for details.

R_a	R_b	V	$\alpha^{(1)}_{1s}$	$\alpha^{(1)}_{2s}$	$\alpha^{(1)}_{3s}$	$\alpha^{(1)}_{4s}$	$\alpha^{(1)}_{2p}$	$\alpha^{(1)}_{3d}$
0	1	1	0.02879202[a]	0.00441401	0.00188747	0.00105362	0.01715126	0.00894345
0.1	1	0.999	0.04759422[a]	0.02720296	0.02357306	0.02219162	0.01004334	0.00815930
0.2	1	0.992	0.07284697[a]	0.05487311	0.05124972	0.04988689	0.00583028	0.00565908
0.5	1	0.875	0.20188347[a]	0.19133640	0.18923265	0.18848057	0.00083203	0.00083480
0.8	1	0.488	0.43528355	0.43282926	0.43236928	0.43220786	0.00002109	0.00002109
0	2	8	0.34255811[b]	−0.0168850	−0.00436115	−0.00163080	0.30828166	0.15185462
0.1	2	7.999	0.51258523[b]	0.22332074	0.19042816	0.17549582	0.21885819	0.149192555
0.5	2	7.875	1.37743250[b]	1.14984366	1.09461376	1.07278640	0.07037524	0.07079627
1	2	7	3.22129727[b]	3.0635182	3.02914678	3.01659244	0.01330690	0.01335487
1.2	2	6.272	4.25881264	4.1404792	4.11614071	4.10740597	0.00542262	0.00542936
1.5	2	4.625	6.20198032	6.1449042	6.13390400	6.13002002	0.00082430	0.00082441
1.8	2	2.168	8.67861281	8.6676719	8.66563354	8.66491917	0.00002106	0.00002108
0	5	125	3.42245422	−21.10657309	−5.69164044	−2.65407833	18.08924616	7.21196971
1	5	124	38.3097689	34.92837261	32.75186815	31.71727294	3.57857074	3.72434520
2	5	117	90.3835855	85.34545419	83.48828979	82.73474712	1.08353807	1.09660163
2.5	5	109.375	124.798441	119.92301897	118.49342276	117.94158361	0.51897086	0.52129425
3	5	98	165.908991	161.85822945	160.86291102	160.49304359	0.21171092	0.21200753
4	5	61	272.010054	270.53059396	270.23821589	270.13447254	0.01317982	0.01318049
4.5	5	33.875	339.006228	338.58155287	338.50168038	338.47363247	0.0008232	0.00082310
0	10	1000	4.49681419[c]	37.23973625	−376.86905909	−143.24860953	793.3231266	171.8366872
0.5	10	999.875	57.8605712	87.17950256	107.31693132	110.54059768	107.3856268	152.9035064
1	10	999	163.642519	277.6753968	254.03479328	238.63416165	80.69486982	113.7656686
2	10	992	485.283240[c]	583.9858189	540.82756495	518.84632115	52.316849	60.8621082
3	10	973	900.888347[c]	936.7193051	895.52440838	876.03156272	31.4884761	33.2715571
5	10	875	1969.35287[c]	1925.755087	1900.38211125	1889.89454238	8.2726984	8.32191160
7	10	657	3430.37098[c]	3390.605514	3380.46513160	3376.69265692	1.0688590	1.06926410
9.5	10	142.625	6023.026447	6021.229170	6020.89385098	6020.77626011	0.0008310	0.000836
0	∞		4.50000000[d]	120.0000000[d]	1012.5000000[d]	4992.0000000[d]	176.0000000[d]	1863.0000000[d]
0.1	∞		11.0436170	−832.82391	−19470.0124	−157741.0999	551.13773744	1862.6259940
0.5	∞		62.0058551	1191.23431	6853.5900	20163.4888	300.6834286	24243.2503
1	∞		206.890953	3978.47424	29050.9501	131865.02	311.4948323	7601.124077
2	∞		928.385427	13601.4303	89661.9116	389708.7	466.836635	3831.84946
5	∞		10180.1611	90653.1600	458038.2	1685829.4	1425.94246	3701.13787
7	∞		27077.8811	199530.231	900453.4		2448.04066	4859.03373
8	∞		40427.5127	276691.870			3080.4164	5613.81181
9	∞		57889.5118	371559.069	1538454.7		3797.0113	6473.34645
10	∞		80147.5187	486116.385	1941232.3		4600.2812	7434.64009

[a]Literature results [3] for $\alpha^{(1)}_{1s}$ ($R_b = 1$) at $R_a = 0, 0.1, 0.2, 0.5$ are 0.0284, 0.0473, 0.0716, 0.2000.
[b]Literature results [3] for $\alpha^{(1)}_{1s}$ ($R_b = 2$) at $R_a = 0, 0.1, 0.5, 1.0$ are 0.3405, 0.5095, 1.3588, 3.2041.
[c]Literature results [3] for $\alpha^{(1)}_{1s}$ ($R_b = 10$) at $R_a = 0, 2, 3, 5, 7$ are 4.4851, 474.3865, 880.0750, 1962.3385, 3394.0953.
[d]Literature results [82] for $\alpha^{(1)}_{1s}, \alpha^{(1)}_{2s}, \alpha^{(1)}_{3s}, \alpha^{(1)}_{4s}, \alpha^{(1)}_{2p}, \alpha^{(1)}_{3d}$ in the FHA are 4.5, 120, 1012.5, 4992, 176, 1863.

showing distinct changes with r_c, offering both (+)ve and (−)ve values. A straightforward inference is that, with the growth in r_c, $\alpha^{(1)}$ in a given state with an arbitrary ℓ increases as r_c proceeds towards the respective FHA limit. At $r_c = 2, 5$, the $2s$, $3s$, $4s$ states offer (−)ve polarizability; the same is also found for latter two states at $r_c = 10$.

(ii) *SCHA*. In this situation, the characteristics of $\alpha^{(1)}$ change with ℓ. For s-wave states, (at a fixed R_b) it increases with R_a. A resembling nature in $\alpha^{(1)}$ is also achieved by varying R_b while keeping R_a fixed. These two outcomes suggest that it depends on the (R_a, R_b) pair, but not on their difference, ΔR. In contrast, for $\ell \neq 0$ states, at a specific R_b, it decreases with R_a, but for a given R_a, it increases with R_b. Thus, in this scenario, $\alpha^{(1)}$ is controlled by all three quantities, R_a, R_b, and ΔR.

(iii) *LCHA*. In $\ell = 0$ states, it grows with R_a, but a *zigzag* pattern is seen for $2p$ and $3d$.

Table IV shows that, for s waves, at a fixed R_b, $\alpha^{(1)}$ progresses with R_a. However, after some characteristic R_a, it prevails over volume, given in the third column. According to the *Herzfeld criterion* [3,83], an insulator → metal conversion occurs under the condition

$$\frac{4\pi}{3}V \leqslant \left(\frac{4\pi}{3}\right)\alpha^{(1)}, \quad V = \left(R_b^3 - R_a^3\right) \leqslant \alpha^{(1)}. \tag{17}$$

TABLE V. Estimated $R_a = R_m$ at 10 selected R_b for the $1s, 2s, 3s, 4s$ states in the SCHA. See the text for details.

	$R_a = R_m$			
R_b	$1s$	$2s$	$3s$	$4s$
1	0.81776350	0.81844574	0.818572206	0.818616480
2	1.380547989[a]	1.386963908	1.388196667	1.388631630
3	1.78705451[a]	1.806803958	1.810946733	1.812435703
4	2.091846379[a]	2.130115046	2.139377180	2.1427985178
5	2.329536517[a]	2.385985164	2.40275065	2.4091529423
6	2.524110980[a]	2.591789087	2.618502823	2.629078449
7	2.692788378[a]	2.758505970	2.7976385904	2.813701635
8	2.847829929[a]	2.893365851	2.9474474821	2.9704167040
9	2.997651615[a]	3.00123877	3.0729537329	3.104343080
10	3.147719215[a]	3.08540221	3.177732377	3.219149730

[a]For $R_b = 2, 3, 4, 5, 6, 7, 8, 9, 10$, literature results [3] for R_m are 1.73,2.08,2.34,2.54,2.71,2.87,3.01,3.15,3.29, respectively.

Now, applying the above criterion, one can easily discern that in the SCHA a metallic character can be observed in all the s states. This feature was reported before [3] for the *ground state* of a SCHA. This work, however, shows that it can also be extended to excited states with $\ell = 0$. The threshold R_a at which $\alpha^{(1)}$ surpasses V (symbolized as R_m) is produced in Table V for four s states at 10 selected R_b (1,2,3,4,5,6,7,8,9,10). For a given $\alpha^{(1)}$, R_m tends to assume larger values with the growth of R_b. Moreover, with an increase of R_b, the metallic zone $(R_b - R_m)$ is extended. Results from the literature are quoted in the footnote, which shows decent qualitative agreement.

We present a cross section of the results for 2^k-pole polarizabilities ($k = 2, 3, 4$) of the $1s$ state in the CHA, SCHA, and LCHA in Fig. 6. Figures 6(a), 6(b) and 6(c) represent them for quadrupole, octupole, and hexadecapole polarizabilities. The bottom row (with panels labeled I), for the CHA, indicates that, for all k, $\alpha^{(k)}$ sharply increases with r_c before finally merging to the respective FHA limit. Parallel results for the SCHA against R_a are depicted in the panels labeled II, with R_b fixed at 5, reflecting a steady monotonic growth. Similarly, the panels labeled III offer the SCHA results while varying both R_a and R_b but $\Delta R = 1$ constant. However, here also, the monotonic increasing trend is maintained for all k, as in the previous SCHA situation. Finally, the topmost panels (labeled IV) show the respective plots in the case of the LCHA and bear a close resemblance to the SCHA scenario.

C. Information entropy

Now we will present some results for information entropy. A few points are worth noting first. The net information measure in r and p space in a central potential may be separated into two parts, viz., (i) radial and (ii) angular contributions, as mentioned in Eq. (10). The latter remains unchanged in the two conjugate spaces in these systems; furthermore, the same is true for different confinement situations of the GCHA, modeled with various boundary conditions. Moreover, we have opted to set the magnetic quantum number m to zero, unless stated otherwise. In all reported cases, $S_{\mathbf{r}} + S_{\mathbf{p}} = S_t$ satisfy the lower bound: $3(1 + \ln \pi)$.

Representative $S_{\mathbf{r}}$ and $E_{\mathbf{r}}^O$ for the $1s$ state in the GCHA are given in Table VI. The SCHA results provided for four R_b (1,2,5,10) show that $S_{\mathbf{r}}$ progresses with R_a to reach a plateau and then declines. That means that, for each R_b, there is a range of R_a where $S_{\mathbf{r}}$ grows with a decrease in ΔR. However, the changes in $S_{\mathbf{p}}$ are not so straightforward. At $R_b = 1$, it increases with a rise in R_a, while at $R_b = 2$, 5, or 10, it passes through a shallow minimum. Thus, with a reduction in the shell radius (ΔR), $S_{\mathbf{r}}$ and $S_{\mathbf{p}}$ increase and decrease, signifying a gain and loss in uncertainty in the r and p spaces. This trend is the reverse of what is observed in the CHA [25], where a shortening of r_c causes a fall and rise in $S_{\mathbf{r}}$ and $S_{\mathbf{p}}$. However, at a fixed R_a, their sum, $S_{\mathbf{r}} + S_{\mathbf{p}} = S_t$, always increases with the growth of R_b. As usual, $E_{\mathbf{r}}^O$ and $E_{\mathbf{p}}^O$ show an opposite trend with respect to $S_{\mathbf{r}}$ and $S_{\mathbf{p}}$. At a fixed R_b, $E_{\mathbf{r}}^O$ collapses to a flat minimum, and $E_{\mathbf{p}}^O$ increases up to a shallow maximum. Moreover, E_t^O always declines with an increase in R_a. This pattern complements the outcome of S. The bottom of Table VI provides results for the LCHA. Unlike the SCHA, here, the trend of $S_{\mathbf{r}}$ and $S_{\mathbf{p}}$ is very straightforward; with the growth in R_a, the former increase, while the latter decreases. In contrast, $E_{\mathbf{r}}^O$ reduces, and $E_{\mathbf{p}}^O$ advances with a change in R_a. Further, S_t decays and reaches a shallow minimum, and E_t^O approaches a flat maximum.

The above results for the SCHA and LCHA in the ground state drive us to extend the study to $\ell \neq 0$ states. Thus, we present $S_{\mathbf{r}}$ for the first five circular (nodeless) states in the SCHA and LCHA in Fig. 7. Rows I, II, and III correspond to the SCHA, the SCHA with fixed $\Delta R = 1$, and the LCHA; Figs. 7(a)–7(e) show states with $\ell = 0$–4, respectively. Like the previous plots for $f^{(k)}$ and $\alpha^{(k)}$, here also, SCHA graphs are presented in two separate forms. First, $S_{\mathbf{r}}$ is plotted against R_a while keeping R_b fixed at 5 in the bottom row. For $1s$, a distinct dome-shaped structure appears, while for the remaining states, the initial shape is partially lost, retaining the sharp decay at large R_a. Second, in the middle row, $S_{\mathbf{r}}$ is shown as a function of R_a while keeping ΔR constant at 1. In all five states $S_{\mathbf{r}}$ firmly progresses with R_a. The top row displays the respective plot for the LCHA. For $1s$ [Fig. 7(a)], it grows uninterruptedly. For other states, in the beginning, there is a

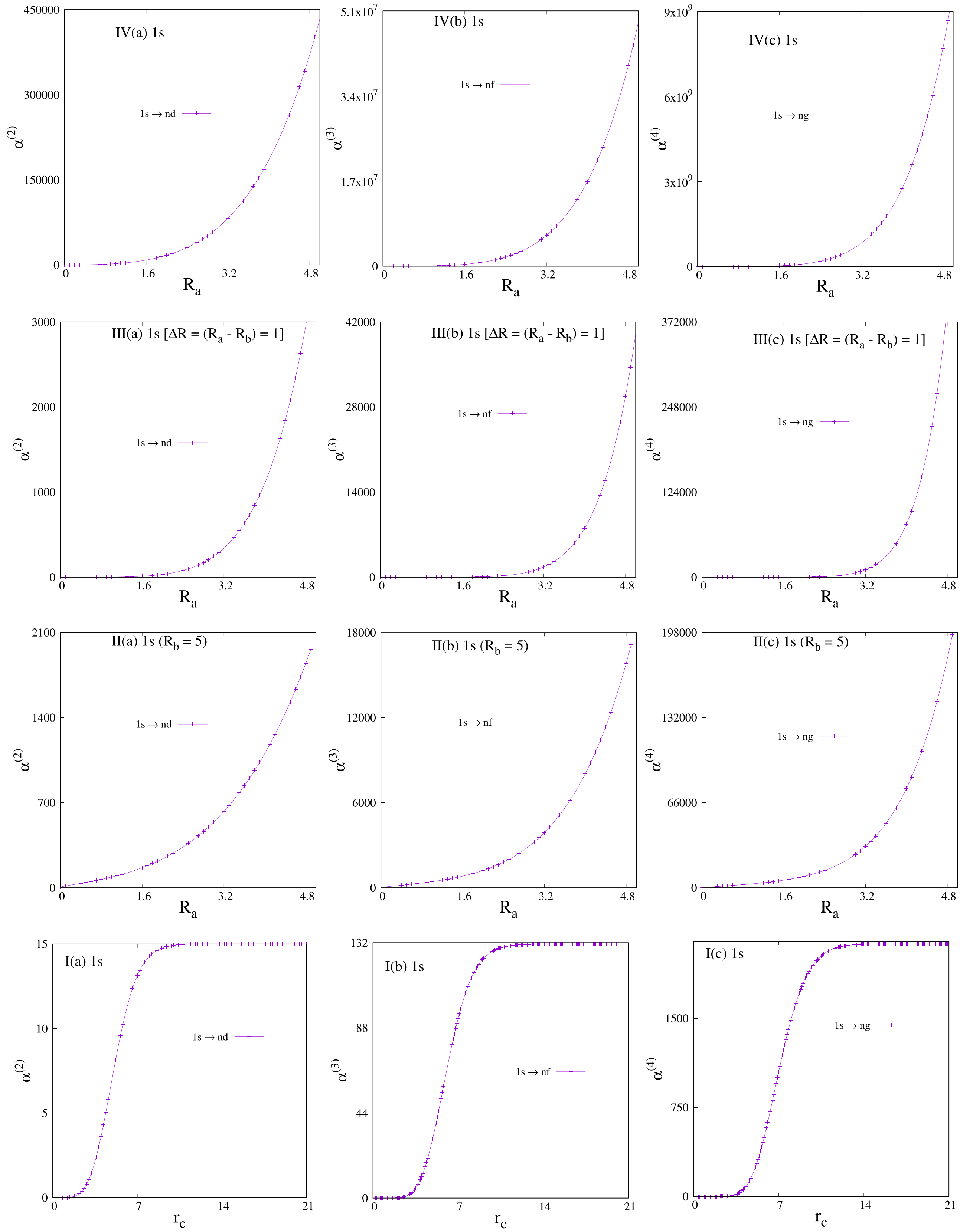

FIG. 6. (a)–(c) Plots of $\alpha^{(k)}$ ($k = 2$–4) in the $1s$ state in the GCHA. In the CHA (panel I) they are plotted as a function of r_c (in a.u.). In panels (II) and (IV) they are shown against R_a for the SCHA and LCHA. In panel (III), they are given for the SCHA, considering $\Delta R = (R_b - R_a) = 1$. See the text for details.

TABLE VI. S and E^O for the ground state in the GCHA. See the text for details.

R_a	R_b	$S_{\mathbf{r}}$	$S_{\mathbf{p}}$	$S_t = S_{\mathbf{r}} + S_{\mathbf{p}}$	$E^O_{\mathbf{r}}$	$E^O_{\mathbf{p}}$	$E^O_t = E^O_{\mathbf{r}} E^O_{\mathbf{p}}$
0	1	0.52903053	6.0114	6.5404	0.84791729	0.00364537	0.00309098
0.1	1	0.77666759	6.040785	6.817452	0.56908172	0.004180	0.002378
0.2	1	0.89751313	6.23932	7.13683	0.47934610	0.004133	0.001981
0.5	1	0.93965484	7.35022	8.28987	0.43687955	0.0025784	0.0011264
0.8	1	0.40237874	9.9389	10.3412	0.73903793	0.00056417	0.00041694
0	2	2.39666961	4.09171	6.48837	0.14785297	0.0254120	0.0027572
0.1	2	2.66321083	3.93985	6.60306	0.09448635	0.030017	0.002836
0.5	2	3.00050972	4.30210	7.30261	0.05789843	0.03171950	0.00183651
1	2	3.01785556	5.28370	8.30155	0.05469677	0.020779	0.001136
1.2	2	2.93197744	5.88332	8.81529	0.05923939	0.014951	0.000885
1.5	2	2.64748816	7.20552	9.85300	0.07834727	0.0068029	0.0005329
1.8	2	1.89807736	9.88472	11.78280	0.16543757	0.00124238	0.0002055
0	5	4.01744418	2.5243610	6.5418051	0.04217574	0.16706123	0.00704593
1	5	5.63473499	1.4621	7.0968	0.00432817	0.490356	0.002122
2	5	5.78652038	2.06176	7.84828	0.00347700	0.404385	0.001406
2.5	5	5.76289185	2.52188	8.28477	0.00351784	0.321734	0.001131
3	5	5.67961160	3.12263	8.80224	0.00379731	0.231656	0.000879
4	5	5.23062327	5.0882	10.3188	0.00591282	0.071235	0.000421
4.5	5	4.64694680	7.1204	11.7673	0.01058804	0.01925812	0.00020390
0	10	4.14461075	2.42193665	6.5665474	0.03978966	0.20886414	0.00831063
0.5	10	6.22396712	0.317019	6.540986	0.00339560	1.3629551	0.00462805
1	10	6.96632717	−0.31664	6.64968	0.00140630	2.47609	0.00348
2	10	7.56814293	−0.5044	7.0637	0.00065283	3.5697296	0.0023304
3	10	7.77837713	−0.3423	7.4360	0.00049254	3.621882	0.001783
5	10	7.83556437	0.4567	8.2922	0.00044356	2.561340	0.001136
7	10	7.59776142	1.8617	9.4594	0.00055562	1.154784	0.000641
9.5	10	6.08547241	7.057	13.142	0.00251172	0.040427	0.000101
0	∞	4.14472988	2.42186234	6.56659222	0.03978873	0.20897494	0.00831484
0.1	∞	4.90515587	1.6122737	6.51742957	0.01564470	0.41905958	0.01912784
0.5	∞	6.26312315	0.28264261	6.54576576	0.00333958	1.48254647	0.00495108
1	∞	7.15077757	−0.521160	6.629617	0.00126846	3.4015178	0.00431468
2	∞	8.21112685	−1.436799	6.774327	0.00040908	9.1531967	0.0037443
5	∞	9.84346840	−2.789102	7.054366	0.00007410	41.251854	0.0030567
7	∞	10.49963587	−3.29565	7.20398	0.00003758	72.517286	0.002725
8	∞	10.76761132	−3.4717	7.2959	0.00002851	88.50086	0.002523
9	∞	11.00741529	−3.60159	7.40582	0.00002228	102.82136	0.002290
10	∞	11.22460206	−3.91190	7.31270	0.00001782	146.1012	0.0026

resistance to change. In other words, it remains invariant up to a certain R_a and then increases.

IV. FUTURE AND OUTLOOK

The incidental degeneracy, multipole oscillator strength, multipole polarizability, Shannon entropy, and Onicescu information energy were investigated for the GCHA model, with special emphasis on the SCHA. The proposed model can explain both *free* and *confined* systems effectively. An in-depth analysis revealed several fascinating features in such systems. The possibility of this degeneracy in Debye and exponential-cosine-screened plasma environments has been established. In the GCHA with an increase in n the number of these degenerate states increases, while at a fixed n, with a growth in ℓ, their count declines. In the confined condition, *negative* polarizability is encountered in the ground and several excited states, which, in agreement with the Herzfeld criterion, suggests a metallic character. Simplified analytical expressions for $f^{(k)}$ and $\alpha^{(k)}$ in the FHA were reported. The impact of R_a, R_b, and ΔR on the spectroscopic and density-dependent properties was examined. Similar calculations for other central potentials are highly desirable. Particularly, it is necessary to verify the existence of such degeneracy by imposing *shell confinement* on other quantum chemical systems. Investigation of the Hellmann-Feynman theorem in the context of a SCHA is desirable. Further, an exploration of the two-photon transition amplitude, photoionization cross section, and relative information in the GCHA model would provide critical insight. Apart from that, it would be interesting to extend the shell-confinement model to many-electron atoms.

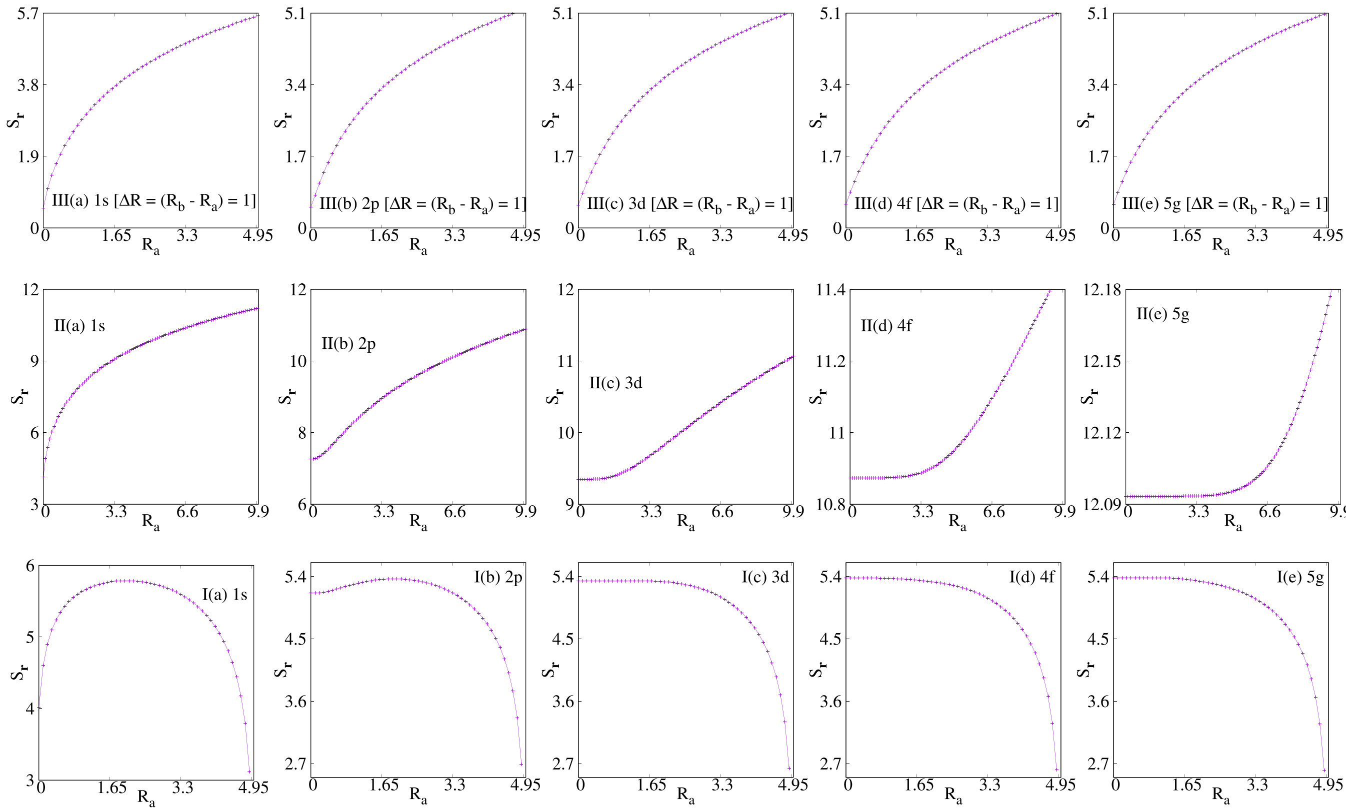

FIG. 7. Plot of $S_{\mathbf{r}}$ as a function of R_a (in a.u.) for $1s, 2p, 3d, 4f, 5g$ states in (I) the SCHA with $R_b = 5$ and (II) the SCHA with ΔR fixed at 1 a.u. (III) LCHA. See the text for details.

ACKNOWLEDGMENTS

Financial support from BRNS, India (Sanction Order No. 58/14/03/2019-BRNS/10255), is gratefully acknowledged. Partial financial support from SERB, India (Grant No. CRG/2019/000293), is also appreciated. N.M. thanks CSIR, New Delhi, India, for support through a senior research associateship (Pool No. 9033A). The authors acknowledge valuable discussion with Prof. K. D. Sen. The authors thank two anonymous referees for their constructive comments.

APPENDIX: MULTIPOLE OSCILLATOR STRENGTH AND POLARIZABILITY IN FHA

Here, we present the *first* transition corresponding to the respective selection rule for $k = 1, 2, 3, 4$. The remaining results are provided in the Supplemental Material [84].

1. Dipole oscillator strength and polarizability

The selection rule is $\Delta\ell = \pm 1$. In s states, it changes to $\Delta\ell = 1$. However, in $\ell \neq 0$ states, $\alpha_{n\ell}^{(1)} = \alpha_{n\ell}^{(1)}(\ell - 1) + \alpha_{n\ell}^{(1)}(\ell + 1)$. The expressions for $f_{(1s\to np)}^{(1)}(Z)$ and $f_{(2p\to ns)}^{(1)}(Z)$ are found as

$$f_{(1s\to np)}^{(1)}(Z) = \frac{2^8}{3Z^7}\, n^5\, \frac{(n-1)^{(2n-4)}}{(n+1)^{(2n+4)}}, \quad f_{(2p\to ns)}^{(1)}(Z) = \frac{2^{13}}{27Z^7}\, n^7\, \frac{(n-2)^{(2n-5)}}{(n+2)^{(2n+5)}} \;\; (n \neq 2). \tag{A1}$$

Now, using Eq. (A1) in Eq. (4), we easily get $\alpha_{1s}^{(1)}(p)(Z)$ and $\alpha_{2p}^{(1)}(s)(Z)$ of the FHA. They are obtained as

$$\alpha_{1s}^{(1)}(p)(Z) = \sum_{j=2}^{n} \frac{2^{10}}{3Z^9}\, j^9\, \frac{(j-1)^{(2j-6)}}{(j+1)^{(2j+6)}}, \quad \alpha_{2p}^{(1)}(s)(Z) = \sum_{\substack{j=1\\ j\neq 2}}^{n} \frac{2^{19}}{27Z^9}\, j^{11}\, \frac{(j-2)^{(2j-7)}}{(j+2)^{(2j+7)}}. \tag{A2}$$

2. Quadrupole oscillator strength and polarizability

In this case, the selection rule is $\Delta\ell = 0, \pm 2$. In s states it is $\Delta\ell = 2$. Similarly, in p states $\Delta = 0, 2$. Hence, $\alpha_{n\ell=1}^{(2)} = \alpha_{n\ell}^{(2)}(\ell) + \alpha_{n\ell}^{(2)}(\ell + 2)$. Moreover, for $\ell \geqslant 2$, $\alpha_{n\ell}^{(2)} = \alpha_{n\ell}^{(2)}(\ell - 2) + \alpha_{n\ell}^{(2)}(\ell) + \alpha_{n\ell}^{(2)}(\ell + 2)$.

The closed-form expressions of $f^{(2)}_{(1s\to nd)}(Z)$, $f^{(2)}_{(2p\to np)}$, and $f^{(2)}_{(3d\to ns)}(Z)$ are obtained as

$$f^{(2)}_{(1s\to nd)}(Z) = \frac{2^{12}}{5Z^9}\, n^7\, (n^2-4)\frac{(n-1)^{(2n-6)}}{(n+1)^{(2n+6)}},\quad f^{(2)}_{(2p\to np)}(Z) = \frac{2^{22}}{75Z^9}\, n^9\, (n^2-1)\frac{(n-2)^{(2n-7)}}{(n+2)^{(2n+7)}},$$
$$(2)_{(3d\to ns)}(Z) = \frac{2^{17}3^7}{125Z^9}\, n^{13}\, (n^2-6)^2\frac{(n-3)^{(2n-9)}}{(n+3)^{(2n+9)}}. \tag{A3}$$

Now, applying Eq. (A3) in Eq. (4), we easily get $\alpha^{(2)}_{1s}(d)(Z)$, $\alpha^{(2)}_{2p}(p)(Z)$, and $\alpha^{(2)}_{3d}(s)(Z)$ of the FHA. They take the following forms:

$$\alpha^{(2)}_{1s}(d)(Z) = \sum_{j=3}^{n}\frac{2^{12}}{5Z^{11}}\, j^{11}\, (j^2-4)\frac{(j-1)^{(2j-8)}}{(j+1)^{(2j+8)}},\quad \alpha^{(2)}_{2p}(p)(Z) = \sum_{j=3}^{n}\frac{2^{28}}{75Z^{11}}\, j^{13}(j^2-1)\frac{(j-2)^{(2j-8)}}{(j+2)^{(2j+8)}},$$
$$\alpha^{(2)}_{3d}(s)(Z) = \sum_{\substack{j=1\\ j\neq 3}}^{n}\frac{2^{19}3^{11}}{5^3Z^{11}}\, j^{17}(j^2-6)^2\,\frac{(j-3)^{(2j-11)}}{(j+3)^{(2j+11)}}. \tag{A4}$$

3. Octupole oscillator strength and polarizability

The selection rule is $\Delta\ell = \pm 1, \pm 3$. For $\ell = 0$, $\Delta\ell = 3$. For $\ell = 1$, $\alpha^{(3)}_{n\ell} = \alpha^{(3)}_{n\ell}(\ell+1) + \alpha^{(3)}_{n\ell}(\ell+3)$. Next, for $\ell = 2$, the relation is $\alpha^{(3)}_{n\ell} = \alpha^{(3)}_{n\ell}(\ell-1) + \alpha^{(3)}_{n\ell}(\ell+1) + \alpha^{(3)}_{n\ell}(\ell+3)$. Further, for $\ell \geqslant 3$, $\alpha^{(3)}_{n\ell} = \alpha^{(3)}_{n\ell}(\ell-1) + \alpha^{(3)}_{n\ell}(\ell-3) + \alpha^{(3)}_{n\ell}(\ell+1) + \alpha^{(3)}_{n\ell}(\ell+3)$.

Now, $f^{(3)}_{(1s\to nf)}(Z)$, $f^{(3)}_{(2p\to nd)}(Z)$, $f^{(3)}_{(3d\to np)}(Z)$, and $f^{(3)}_{(4f\to ns)}(Z)$ are written as

$$\begin{aligned}
f^{(3)}_{(1s\to nf)}(Z) &= \frac{9\,2^{12}}{7Z^{11}}\, n^9\, (n^2-4)(n^2-9)\frac{(n-1)^{(2n-8)}}{(n+1)^{(2n+8)}},\\
f^{(3)}_{(2p\to nd)}(Z) &= \frac{2^{27}}{49Z^{11}}\, n^{13}\, (n^2-1)(n^2-16)^2\frac{(n-2)^{(2n-10)}}{(n+2)^{(2n+10)}},\\
f^{(3)}_{(3d\to np)}(Z) &= \frac{2^{18}3^{13}}{5^2\,7^2\,Z^{11}}\, n^{13}\, (n^2-1)(4n^2-9)^2\frac{(n-3)^{(2n-12)}}{(n+3)^{(2n+12)}},\\
f^{(3)}_{(4f\to ns)}(Z) &= \frac{2^{34}}{245Z^{11}}\, n^{15}\, (141n^4 - 3008n^2 + 18\,176)^2\frac{(n-4)^{(2n-13)}}{(n+4)^{(2n+13)}}.
\end{aligned} \tag{A5}$$

Putting Eq. (A5) in Eq. (4), we easily get $\alpha^{(3)}_{4f}(s)(Z)$, $\alpha^{(3)}_{1s}(f)(Z)$, $\alpha^{(3)}_{2p}(d)(Z)$, $\alpha^{(3)}_{3d}(p)(Z)$, and $\alpha^{(3)}_{4f}(s)(Z)$. They have the following forms:

$$\begin{aligned}
\alpha^{(3)}_{1s}(f)(Z) &= \sum_{j=4}^{n}\frac{9\,2^{14}}{7Z^{13}}\, j^{13}\, (j^2-4)(j^2-9)\frac{(j-1)^{(2j-10)}}{(j+1)^{(2j+10)}},\\
\alpha^{(3)}_{2p}(d)(Z) &= \sum_{j=3}^{n}\frac{2^{33}}{49Z^{13}}\, j^{17}(j^2-1)(j^2-16)^2\frac{(j-2)^{(2j-12)}}{(j+2)^{(2j+12)}},\\
\alpha^{(3)}_{3d}(p)(Z) &= \sum_{\substack{j=1\\ j\neq 3}}^{n}\frac{2^{20}3^{17}}{5^2\,7^2Z^{13}}\, j^{17}(j^2-1)(4j^2-9)^2\,\frac{(j-3)^{(2j-14)}}{(j+3)^{(2j+14)}},\\
\alpha^{(3)}_{4f}(s)(Z) &= \sum_{\substack{j=2\\ j\neq 4}}^{n}\frac{2^{44}}{245\,Z^{13}}\, j^{19}(141j^4 - 3008j^2 + 18\,176)^2\,\frac{(j-4)^{(2j-15)}}{(j+4)^{(2j+15)}}.
\end{aligned} \tag{A6}$$

The expression for $\alpha^{(4)}_{n\ell}$ changes with alteration of the ℓ values. These expressions are

$$\begin{aligned}
\ell = 1,\quad \alpha^{(4)}_{n\ell} &= \alpha^{(4)}_{n\ell}(\ell+2) + \alpha^{(4)}_{n\ell}(\ell+4),\\
\ell = 2,\quad \alpha^{(4)}_{n\ell} &= \alpha^{(4)}_{n\ell}(\ell) + \alpha^{(4)}_{n\ell}(\ell+2) + \alpha^{(4)}_{n\ell}(\ell+4),\\
\ell = 3,\quad \alpha^{(4)}_{n\ell} &= \alpha^{(4)}_{n\ell}(\ell-2) + \alpha^{(4)}_{n\ell}(\ell) + \alpha^{(4)}_{n\ell}(\ell+2) + \alpha^{(4)}_{n\ell}(\ell+4),\\
\ell = 4,\quad \alpha^{(4)}_{n\ell} &= \alpha^{(4)}_{n\ell}(\ell-4) + \alpha^{(4)}_{n\ell}(\ell-2) + \alpha^{(4)}_{n\ell}(\ell) + \alpha^{(4)}_{n\ell}(\ell+2) + \alpha^{(4)}_{n\ell}(\ell+4).
\end{aligned} \tag{A7}$$

$f^{(4)}_{(1s\to ng)}(Z)$, $f^{(4)}_{(2p\to nf)}(Z)$, $f^{(4)}_{(3d\to nd)}(Z)$, $f^{(4)}_{(4f\to np)}(Z)$, and $f^{(4)}_{(5g\to ns)}(Z)$ are written as

$$\begin{aligned}
f^{(4)}_{(1s\to ng)}(Z) &= \frac{2^{18}}{9Z^{13}}\, n^{11}\,(n^2-16)(n^2-9)(n^2-4)\,\frac{(n-1)^{(2n-10)}}{(n+1)^{(2n+10)}},\\
f^{(4)}_{(2p\to nf)}(Z) &= \frac{2^{33}}{3^5Z^{13}}\, n^{13}\,(n^2-1)(n^2-9)(7n^2+68)^2\frac{(n-2)^{(2n-12)}}{(n+2)^{(2n+12)}},\\
f^{(4)}_{(3d\to nd)}(Z) &= \frac{2^{20}3^{15}}{35Z^{13}}\, n^{17}\,(n^2-1)(n^2-4)(n^2-21)^2\frac{(n-3)^{(2n-13)}}{(n+3)^{(2n+13)}},\\
f^{(4)}_{(4f\to np)}(Z) &= \frac{2^{43}}{8505Z^{13}}\, n^{17}\,(n^2-1)(31n^4-4768n^2+43\,776)^2\frac{(n-4)^{(2n-15)}}{(n+4)^{(2n+15)}},\\
f^{(4)}_{(5g\to ns)}(Z) &= \frac{2^{21}5^{11}}{7\,3^6Z^{13}}\, n^{19}\,(187n^6-9350n^4+20\,4625n^2+1\,743\,750)^2\frac{(n-5)^{(2n-17)}}{(n+5)^{(2n+17)}}.
\end{aligned}\tag{A8}$$

Now, applying Eqs. (A8) in Eq. (4), we easily obtain $\alpha^{(4)}_{1s}(g)(Z)$, $\alpha^{(4)}_{2p}(f)(Z)$, $\alpha^{(4)}_{3d}(d)(Z)$, $\alpha^{(4)}_{4f}(p)(Z)$, and $\alpha^{(4)}_{5g}(s)(Z)$. They take the following forms:

$$\begin{aligned}
\alpha^{(4)}_{1s}(g)(Z) &= \sum_{i=5}^{n}\frac{2^{20}}{9Z^{15}}\, i^{15}\,(i^2-16)(i^2-9)(i^2-4)\,\frac{(i-1)^{(2i-12)}}{(i+1)^{(2i+12)}},\\
\alpha^{(4)}_{2p}(f)(Z) &= \sum_{j=4}^{n}\frac{2^{39}}{3^5Z^{15}}\, j^{17}(j^2-1)(j^2-9)(7j^2+68)^2\frac{(j-2)^{(2j-14)}}{(j+2)^{(2j+14)}},\\
\alpha^{(4)}_{3d}(d)(Z) &= \sum_{j=3}^{n}\frac{2^{22}3^{19}}{35Z^{15}}\, j^{21}(j^2-1)(j^2-4)(j^2-21)^2\,\frac{(j-3)^{(2j-13)}}{(j+3)^{(2j+13)}},\\
\alpha^{(4)}_{4f}(p)(Z) &= \sum_{\substack{j=2\\ j\neq 4}}^{n}\frac{2^{53}}{8505\,Z^{15}}\, j^{13}(31j^4-4768j^2+43\,776)^2\,\frac{(j-4)^{(2j-13)}}{(j+4)^{(2j+13)}},\\
\alpha^{(4)}_{5g}(s)(Z) &= \sum_{\substack{j=1\\ j\neq 5}}^{n}\frac{2^{27}5^{19}}{7\,3^6\,Z^{15}}\, j^{23}(187j^6-9350j^4+204\,625j^2-1\,743\,750)^2\,\frac{(j-5)^{(2j-19)}}{(j+5)^{(2j+19)}}.
\end{aligned}\tag{A9}$$

[1] W. Grochala, R. Hoffmann, J. Feng, and N. W. Ashcroft, Angew. Chem. Int. Ed. **46**, 3620 (2007).
[2] E. Snider, N. Dasenbrock-Gammon, R. McBride, M. Debessai, H. Vindana, K. Vencatasamy, K. V. Lawler, A. Salammat, and R. P. Dias, Nature (London) **586**, 373 (2020).
[3] K. D. Sen, J. Garza, R. Vargas, and N. Aquino, Phys. Lett. A **295**, 299 (2002).
[4] *Electronic Structure of Quantum Confined Atoms and Molecules*, edited by K. D. Sen (Springer, Cham, 2014).
[5] V. Aquilanti, H. E. Montgomery, Jr., C. N. Ramachandran, and N. Sathyamurthy, Eur. Phys. J. D **75**, 187 (2021).
[6] J.-P. Connerade, Eur. Phys. J. D **74**, 211 (2020).
[7] G. Raggi, A. J. Stace, and E. Bichoutskaia, Phys. Chem. Chem. Phys. **16**, 23869 (2014).
[8] G. Raggi, E. Besley, and A. J. Stace, Philos. Trans. R. Soc. A **374**, 20150319 (2016).
[9] F. J. Dominguez-Gutierrez, P. S. Krstic, S. Irle, and R. Cabrera-Trujillo, Carbon **134**, 189 (2018).
[10] J. Mitroy, M. S. Safronova, and C. W. Clark, J. Phys. B **43**, 202001 (2010).
[11] J. Tiihonen, I. Kylänpää, and T. T. Rantala, J. Chem. Phys. **147**, 204101 (2017).
[12] A. Michels, J. de Boer, and A. Bijl, Physica **4**, 981 (1937).
[13] A. Sommerfeld and H. Welker, Ann. Phys. (Berlin, Ger.) **424**, 56 (1938).
[14] T. Guillot, Planet. Space Sci. **47**, 1183 (1999).
[15] J. Garza, R. Vargas, and A. Vela, Phys. Rev. E **58**, 3949 (1998).
[16] M. Cohen C. Laughlin, and B. L. Burrows, J. Phys. B **35**, 701 (2002).
[17] B. L. Burrows and M. Cohen, Int. J. Quantum Chem. **106**, 478 (2006).
[18] N. Aquino, G. Campoy, and H. E. Montgomery, Jr., Int. J. Quantum Chem. **107**, 1548 (2007).
[19] D. Baye and K. D. Sen, Phys. Rev. E **78**, 026701 (2008).
[20] A. K. Roy, Int. J. Quantum Chem. **115**, 937 (2015).
[21] D. Puertas-Centeno, N. M. Temme, I. V. Toranzo, and J. S. Dehesa, J. Math. Phys. **58**, 103302 (2017).
[22] N. Sobrino-Coll, D. Puertas-Centeno, I. V. Toranzo, and J. S. Dehesa, J. Stat. Mech. (2017) 083102.
[23] H. E. Montgomery, Jr., N. A. Aquino, and K. D. Sen, Int. J. Quantum Chem. **107**, 798 (2007).
[24] N. Mukherjee and A. K. Roy, Phys. Rev. A **99**, 022123 (2019).

[25] N. Mukherjee and A. K. Roy, Int. J. Quantum Chem. **118**, e25596 (2018).
[26] N. Mukherjee, S. Majumdar, and A. K. Roy, Chem. Phys. Lett. **691**, 449 (2018).
[27] L. G. Jiao, L. R. Zan, Y. Z. Zhang, and Y. K. Ho, Int. J. Quantum Chem. **117**, e25375 (2017).
[28] S. Majumdar, N. Mukherjee, and A. K. Roy, Chem. Phys. Lett. **687**, 322 (2017).
[29] N. Mukherjee and A. K. Roy, J. Phys. B **53**, 235002 (2020).
[30] *The Theory of Confined Quantum Systems, Parts I and II*, edited by J. R. Sabin, E. Brändas, and S. A. Cruz, Advances in Quantum Chemistry Vols. 57 and 58 (Academic Press, Cambridge, MA, 2009).
[31] *Statistical Complexity: Applications in Electronic Structure*, edited by K. D. Sen (Springer, Berlin, 2012).
[32] L. R. Zan, L. G. Jiao, J. Ma, and Y. K. Ho, Phys. Plasmas **24**, 122101 (2017).
[33] S. J. C. Salazar, H. G. Laguna, B. Dahiya, V. Prasad, and R. P. Sagar, Eur. Phys. J. D **75**, 127 (2021).
[34] J.-H. Ou and Y. K. Ho, Int. J. Quantum Chem. **119**, e25928 (2019).
[35] Y. Y. He, L. G. Jiao, A. Liu, Y. Z. Zhang, and Y. K. Ho, Eur. Phys. J. D **75**, 126 (2021).
[36] C. Yadav, S. Lumb, and V. Prasad, Eur. Phys. J. D **75**, 21 (2021).
[37] L. Zhu, Y. Y. He, L. G. Jiao, Y. C. Wang, and Y. K. Ho, Int. J. Quantum Chem. **120**, e26245 (2020).
[38] C. Y. Lin and Y. K. Ho, Few-Body Syst. **54**, 425 (2013).
[39] K. D. Sen, J. Chem. Phys. **122**, 194324 (2005).
[40] M. Cohen and B. L. Burrows, Mol. Phys. **106**, 267 (2008).
[41] K. D. Sen and P. C. Schmidt, Phys. Rev. A **23**, 1026 (1981).
[42] J. G. Kirkwood, Phys. Z. **33**, 57 (1932).
[43] R. A. Buckingham, Proc. R. Soc. London, Ser. A **160**, 94 (1937).
[44] R. M. Sternheimer, Phys. Rev. **96**, 951 (1954).
[45] V. I. Pupyshev and H. E. Montgomery, Jr., Int. J. Quantum Chem. **119**, e25887 (2019).
[46] E. M. Nascimento, F. V. Prudente, M. N. Guimaraes, and A. M. Maniero, J. Phys. B **44**, 015003 (2011).
[47] A. L. Efros and D. J. Nesbitt, Nat. Nanotechnol. **11**, 661 (2016).
[48] Z. Fei, Z. Wang, D. Li, F. Xue, C. Cheng, Q. Liu, X. Chen, M. Cui, and X. Qiao, Nanoscale **13**, 10765 (2021).
[49] H. Peng, C. Rao, N. Zhang, X. Wang, W. Liu, W. Mao, L. Han, P. Zhang, and S. Dai, Angew. Chem., Int. Ed. **57**, 8953 (2018).
[50] C. Rao, C. Peng, H. Peng, L. Zhang, W. Liu, X. Wang, N. Zhang, and P. Wu, ACS Appl. Mater. Interfaces **10**, 9220 (2018).
[51] T. Raj kumar, G. Gnana kumar, and A. Manthiram, Adv. Energy Mater. **9**, 1803238 (2019).
[52] Y. Lai, W. Xia, J. Li, J. Pan, C. Jiang, Z. Cai, C. Wu, X. Huang, T. Wang, and J. He, Electrochim. Acta **375**, 137966 (2021).
[53] M. Fan, D. Liao, M. F. Aly Aboud, I. Shakir, and Y. Xu, Angew. Chem. Int. Ed. **59**, 8247 (2020).
[54] A.-C. Shi and B. Li, Soft Matter **9**, 1398 (2013).
[55] M. R. Khadilkar and A. Nikoubashman, Soft Matter **14**, 6903 (2018).
[56] L. Qin, C. Li, X. Li, X. Zhang, C. Shen, Q. Meng, L. Shen, Y. Lu, and G. Zhang, J. Mater. Chem. A **8**, 1929 (2020).
[57] M. Zhang, C. Xiao, X. Yan, S. Chen, C. Wang, R. Luo, J. Qi, X. Sun, L. Wang, and J. Li, Environ. Sci. Technol. **54**, 10289 (2020).
[58] D. E. Hastings and H. D. H. Stöver, ACS Appl. Polym. Mater. **1**, 2055 (2019).
[59] G. Gnana kumar, S.-H. Chung, T. Raj kumar, and A. Manthiram, ACS Appl. Mater. Interfaces **10**, 20627 (2018).
[60] W. Shuang, H. Huang, L. Kong, M. Zhong, A. Li, D. Wang, Y. Xu, and X.-H. Bu, Nano Energy **62**, 154 (2019).
[61] J. Wang, L. Zhu, F. Li, T. Yao, T. Liu, Y. Cheng, Z. Yin, and H. Wang, Small **16**, 2002487 (2020).
[62] A. K. Roy, Mod. Phys. Lett. A **29**, 1450104 (2014).
[63] A. K. Roy, J. Math. Chem. **52**, 1405 (2014).
[64] A. K. Roy, Mod. Phys. Lett. A **29**, 1450042 (2014).
[65] S. Majumdar and A. K. Roy, Quantum Rep. **2**, 189 (2020).
[66] S. Majumdar and A. K. Roy, Int. J. Quantum Chem. **121**, e26630 (2021).
[67] M. Das, Phys. Plasmas **19**, 092707 (2012).
[68] A. Dalgarno, Adv. Phys. **11**, 281 (1962).
[69] L. Zhu, Y. Y. He, L. G. Jiao, Y. C. Wang, and Y. K. Ho, Phys. Plasmas **27**, 072101 (2020).
[70] I. Bialynicki-Birula and J. Mycielski, Commun. Math. Phys. **44**, 129 (1975).
[71] J. S. Shiner, M. Davison, and P. T. Landsberg, Phys. Rev. E **59**, 1459 (1999).
[72] A. Solyu, Phys. Plasmas **19**, 072701 (2012).
[73] L. G. Jiao, Y. Y. He, Y. Z. Zhang, and Y. K. Ho, J. Phys. B **54**, 065005 (2021).
[74] S. Paul and Y. K. Ho, Phys. Rev. A **79**, 032714 (2009).
[75] M. K. Bahar and A. Solyu, Phys. Plasmas **21**, 092703 (2014).
[76] M. K. Bahar, A. Soylu, and A. Poszwa, IEEE Trans. Plasma Sci. **44**, 2297 (2016).
[77] Y.-D. Jung, Phys. Plasmas **2**, 332 (1995).
[78] Y.-D. Jung and J.-S. Yoon, J. Phys. B **29**, 3549 (1996).
[79] M. Y. Song and Y.-D. Jung, J. Phys. B **36**, 2119 (2003).
[80] C. Y. Lin and Y. K. Ho, Eur. Phys. J. D **57**, 21 (2010).
[81] C. Y. Lin and Y. K. Ho, Comput. Phys. Commun. **182**, 125 (2011).
[82] D. Baye, Phys. Rev. A **86**, 062514 (2012).
[83] K. F. Herzfeld, Phys. Rev. **29**, 701 (1927).
[84] See Supplemental Material at http://link.aps.org/supplemental/10.1103/PhysRevA.104.042803 for analytical closed from expression of multipole polarizabilites in *Free H*-atom.